GEOPHYSICAL FAULT MAPPING USING THE MAGNETIC METHOD AT HICKORY SANDSTONE AQUIFER, LLANO UPLIFT, TEXAS

A Thesis

by

ANTÓNIO DO NASCIMENTO PEREIRA

Submitted to the Office of Graduate Studies of
Texas A&M University
in partial fulfillment of the requirements for the degree of

MASTER OF SCIENCE

Approved by:

Chair of Committee,	Mark E. Everett
Co-Chair of Committee,	Yuefeng Sun
Committee Member,	David S. Schechter
Department Head,	John R. Giardino

May 2013

Major Subject: Geophysics

ABSTRACT

A magnetic study over a 95 m × 150 m area of the Hickory sandstone aquifer in central Texas was carried out as part of multitechnique geophysical investigation that included ground penetrating radar (GPR), electromagnetic (EM), seismic and seimoelectric. In geophysical exploration, the magnetic method can be utilized as an alternative to more expensive methods, such as seismic or it can be used to complement other methods. In this thesis, the magnetic method is applied to estimate the location of a previously mapped fault by Texas A&M geology students, and it is used to estimate the magnetic susceptibility contrast of the targeted fault. The main challenge of this study is imaging shallow faults using the geophysical magnetic method in a fractured aquifer with widely-scattered distribution of iron bearing rocks as in the case of the Hickory sandstone aquifer.

A Geometric—G858 Cesium vapor magnetometer was used to collect magnetic data. The data consisted of 19 north-south and 1 east-west lines acquired in October and November of 2012. Elementary data processing such as diurnal correction, regional correction, reduction to pole (RTP) filter, Euler deconvolution, forward modeling and inversion were employed to characterize the faulted zone. This faulted zone separates granite basement rocks from the Hickory sandstone. As a result, this study emphasizes that Euler deconvolution applied to RTP-filtered data increases the interpretability of geological and structural contacts. The results of the magnetic method have been compared to results of GPR, EM and seismoelectric methods. Understanding the magnetic mineralogy of rocks and their properties can improve the geological interpretation of magnetic surveys.

DEDICATION

To my parents, Josefa Nascimento and Kasongo Pereira. May you be honered with this work.

ACKNOWLEDGEMENTS

It is imperative to recognize and acknowledge key individuals and thank them for their support, encouragement, help and examples.

My sincere appreciation goes to my academic advisor Dr. Mark Everett for his constant guidance throughout my research and graduate program. His time and support played a crucial role in completion of this work, he has been fundamental to my growth as a geophysicist.

I would like to express my gratitude to my former academic advisor Dr. Luc Ikelle for mentoring me in the earlier stages of my academic program.

My appreciation also goes to my graduate committee members Dr. Yuefeng Sun and Dr. David Schechter, for their comments and valuable time.

My deep appreciation also goes to the employees of Mason Mountain Wildlife Management Area for their hospitality and help in the field.

I am thankful for the funding provided by Halliburton in the form of a scholarship, and the Department of Geology & Geophysics at Texas A&M University for GAT assistantship.

I would like to thank my family for their prayers and encouragement. Foremost, my love Winnie. My brothers and sisters who have been taking care of me for as far as I can remember. My aunties and uncles for being always ready to help any time I needed. And last but not the least, I would like to thank my friends and colleagues for their camaraderie. Especially my friend Helio Boy for helping me with data collection.

NOMENCLATURE

EM	Electromagnetic
GPR	Ground Penetrating Radar
IGRF	International Geomagnetic Reference Field
RTP	Reduction to pole
MMWMA	Mason Mountain Wildlife Management Area
WMA	Wildlife Management Area
$\nabla\cdot$	The divergence operator
$\nabla\times$	The curl operator
$\mathbf{B}$	Magnetic field or,
	Magnetic induction or,
	Magnetic field density or,
	Magnetic flux density
$\mathbf{E}$	Electric field intensity
$\mathbf{H}$	Magnetic field intensity
$\mathbf{J}$	Magnetizing field,
μ_0	Permeability of free space
M	Magnetic moment
U	Scalar potential

TABLE OF CONTENTS

LIST OF FIGURES

FIGURE Page

LIST OF TABLES

TABLE Page

1. INTRODUCTION

1.1 Introduction

The near—surface structural complexity of the Precambrian Llano Uplift in central Texas provides ideal conditions for geologic and geophysical study. Application of the magnetic method as a geophysical exploration tool has a long history in mining, archeology, and the oil and gas industries [Durrheim and Cooper, 1998]. Rocks containing iron-bearing minerals exhibit magnetic behavior. This behavior can be described mathematically, most importantly using concepts such as the magnetic potential, magnetic field, intensity of magnetization, equivalent dipole moment, and susceptibility [Sharma, 1997]. The magnetic method has previously been used to map fault zones [Grauch et al., 2000; Nasuti et al., 2012; Saheel et al., 2011]. An important objective of a magnetic geophysical investigation is to produce a feasible subsurface distribution of susceptibility that could have engendered the anomalous fields observed in the survey data [Lelievre, 2003].

In this thesis, the magnetic method is used to map a faulted area of the Mason Mountain Wildlife Management Area (MMWMA) in central Texas. The magnetic signature of the fault is expected to be weak with low signal to noise ratio due to the wide distribution of iron bearing rocks near the surface; it is challenging to interpret a magnetic survey under these conditions. Successful imaging of the fault will result in the recommendation of a high resolution magnetic survey of the study area with the purpose of better understanding the subsurface structure. Moreover, an important objective is to map similar faults in similar geological settings elsewhere—not just Llano. The magnetic method is utilized as an alternative or complementary method to more expensive methods such as seismic. The depth to a magnetic structure

is determined by the application of Euler deconvolution to pole-reduced anomalies. Further processing steps include 2—D modeling and inversion. Finally, a comparison is made of the magnetic results to previous results of ground penetrating radar (GPR), seismoelectric, and electromagnetic surveys carried out at or near the study area.

The purpose of the present study is to explore whether geophysical methods, particularly the magnetic technique, can be used to map buried faults in the area. More generally, we want to map faults in fractured rock aquifers. The magnetic data analyzed in this study were acquired along E-W line 0 and N-S lines 0 to 19, parallel to two roads that intersect at the coordinates: latitude +30° 50' 18.60"N, longitude -99° 11' 38.40"W (as shown in Figure 1.1).

1.2 Research methodology

This research was conducted under the following methodology:

1.2.1 Step one—Planning stage

The author in conjunction with the thesis advisor discussed the problem of imaging shallow faults using the geophysical magnetic method in a fractured aquifer with widely-scattered distribution of iron bearing rocks. The Hickory sandstone aquifer in central presents the characteristics above mentioned; therefore, it was chosen as the study site. The faults at this location have been previously mapped by Texas A&M geology students and geophysical surveys using EM and GPR have been conducted. A Literature review was conducted to gain an in-depth understanding of the geologic history of the area as well as the magnetic method in general.

1.2.2 Step two—Survey design & data acquisition

The survey layout was designed in a way that the data acquired would be useful to characterize the subsurface magnetic distribution. Station sampling must be small enough length to mitigate aliasing (less than 0.5 m). The layout consists of 20 N-S magnetic lines crossing the fault, with line spacing 5 m. Additionally, one E-W magnetic line was acquired. The data were acquired using a Geometric—G858 Cesium vapor magnetometer. Magnetic data were also acquired along the same profile as previously-acquired EM and GPR data.

1.2.3 Step three—Data processing & interpretation

A diurnal correction was applied to the data using base station readings, line leveling was accomplished following the steps outlined in the Whitehead [2004] Geosoft technical note. The remaining data reduction were: (1) regional correction; (2) reduction to pole filtering using computer code developed by the thesis advisor based on the Blakely [1995] approach; (3) Euler deconvolution applied to profile data using the Euler software developed by Cooper [2004], while Euler deconvolution applied to gridded data was completed with use of the standard Euler deconvolution from Oasis montaj [Geosoft, 2012]; (4) inversion and modeling were completed using computer programs developed by the thesis advisor. Matlab code written by the author was used to plot the results at each step above mentioned.

1.2.4 Step four—Data analyze

Qualitative interpretation of the magnetic data was made using the results from the previous steps with the objective of estimating the fault location and its susceptibility contrast. To compare with the magnetic data results, previously-acquired GPR, EM and seismoelectric results were also analyzed.

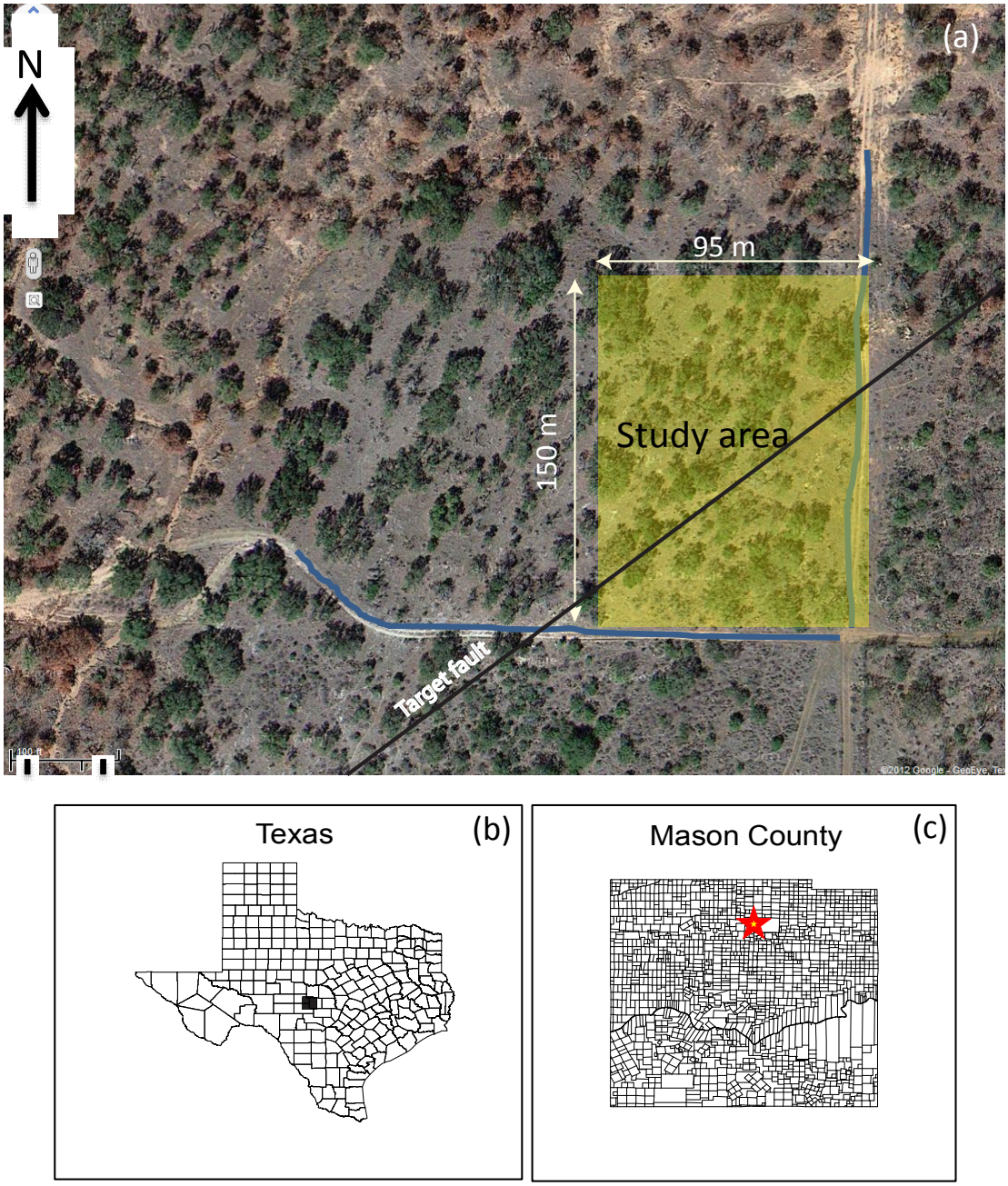

FIG. 1.1. (a) Study area at MMWMA is shown in yellow. The geophysical survey lines 0 west and 1 north are marked in blue. The remaining 18 N-S lines are parallel to line 1; (b) location of Mason County in central Texas; (c) location of the study area in Mason County.

1.3 Geological setting

The study area is located in the Mason Mountain Wildlife Management Area (MMWMA), 12 km north of the town of Mason in central Texas. The site is located on the western margin of the Llano Uplift. The Llano Uplift is characterized by numerous normal faults associated with the Grenville orogeny [Reese, 2000]. The Precambrian rocks of the MMWMA are of Grenville age, roughly 1.0-1.2 Ga [Garrison, 1983; Nelis, 1989]. The Grenville orogeny occurred during the assembly of the supercontinent Rodinia by the collision of Laurentia, i.e. present-day North America, with the African plate [Dalziel and Mosher, 2000]. The region has experienced several regional metamorphic events, the most significant being the Precambrian Grenvillian collision that peaked at 1167 $\pm$12 m.y ago [Garrison, 1983]. The associated regional metamorphism resulted in large scale northwest-southeast folding, followed by granite pluton intrusion about 1056 $\pm$12 m.y ago. These events resulted in uplift and consequently the formation of several strike-slip fault sets that trend east-west and northwest-souteast [Garrison, 1983]. Regional high-angle normal faults with general trend northeast-southwest are ubiquitous in the Llano Uplift. The uplift is a dome-like structure is characterized by 1.0-1.2 Ga Precambrian basement rocks such as gneisses, amphibolites, schists, and granites that subsequently have been exposed by erosion [Barnes and Bell, 1977; Garrison, 1983]. Uplift occurred in several stages during the Precambrian to Miocene interval [Harper, 2011]. Rocks exposed in the study area are predominantly granites, hematitic sandstones, and marbles.

The Middle to Late Cambrian aged Hickory Sandstone is comprised of fluvial, marine, and shoreline transgressive strata deposited in shallow seas [Teran, 2007]. The Hickory Sandstone lies at the base of the Riley Formation, overlain by the Cap Mountain Limestone and Lion Mountain Sandstone [Teran, 2007]. A detailed

description of the Hickory sandstone and the effects of faults on the hydrological system of the Hickory sandstone aquifer can be found in Wilson [2001]. The relevant part of the stratigraphic column of central Texas is shown in Figure 1.2. The target fault of this project has been mapped previously by Texas A&M geology students. Figure 1.3 shows the geological map of MMWMA where the study area and the targeted fault are indicated.

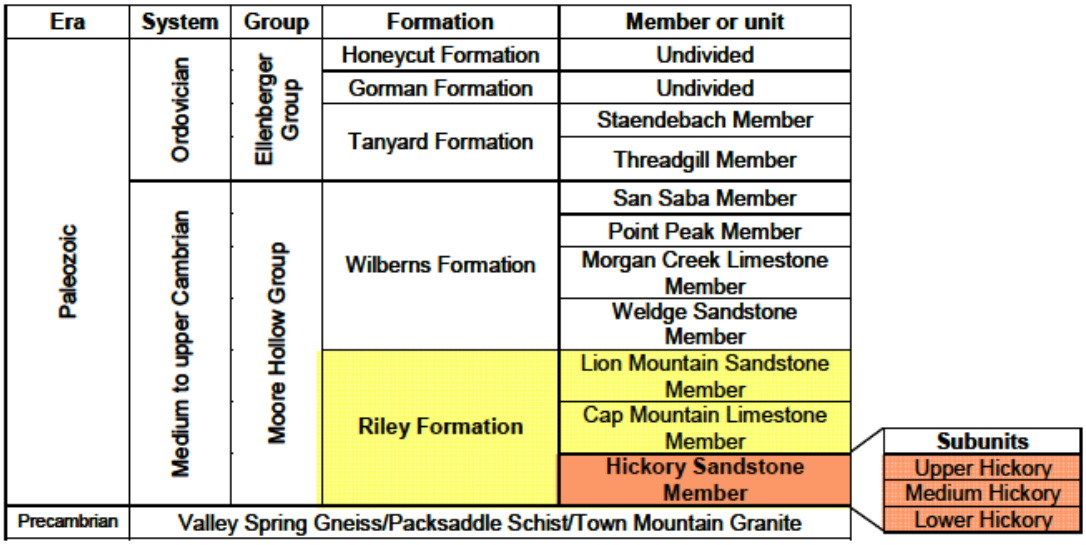

FIG. 1.2. Stratigraphic column of central Texas, USA [Teran, 2007]

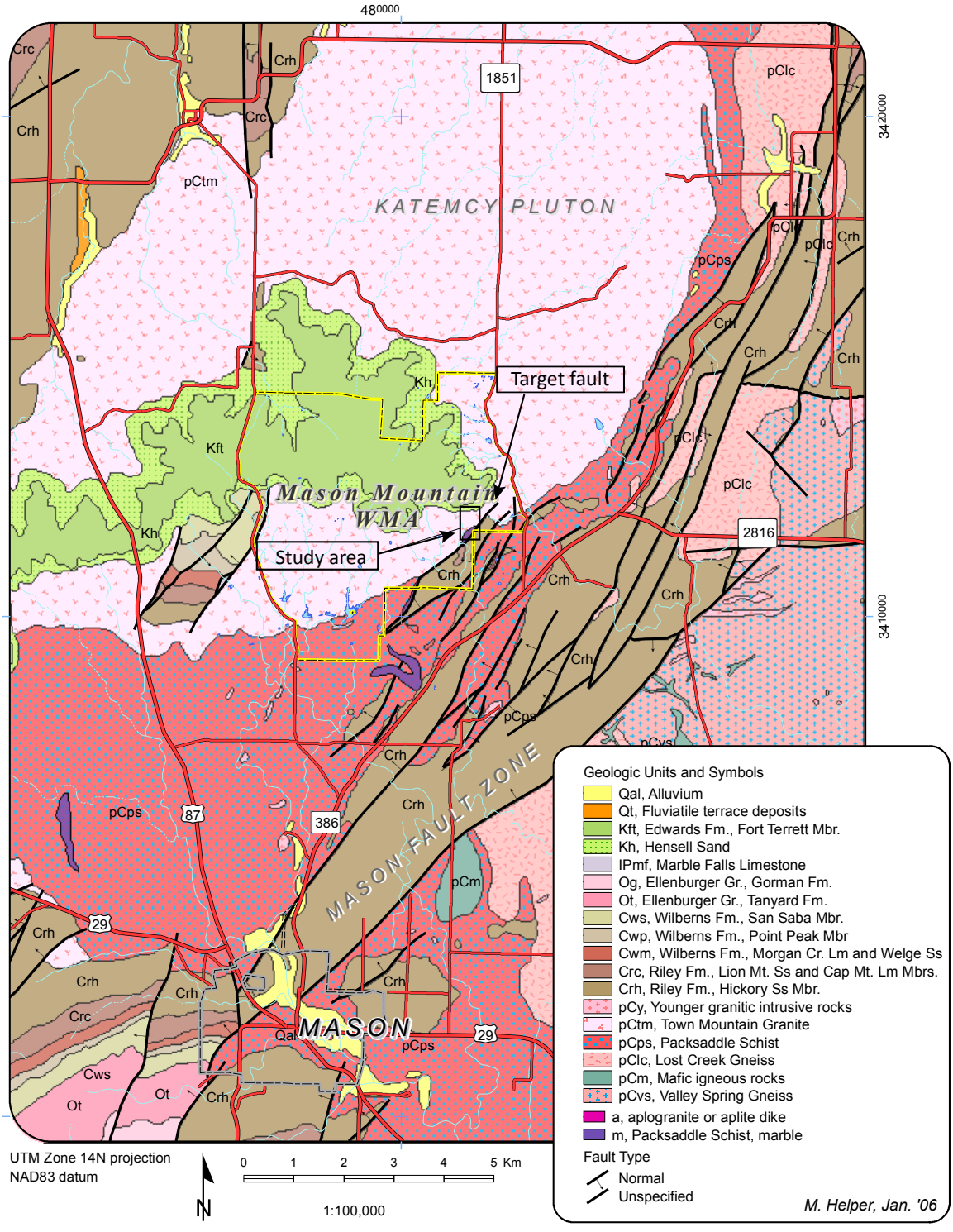

FIG. 1.3. Geologic map of MMWMA. The study area and target fault are indicated in the map [modified from Helper, 2006]

2. BACKGROUND: THE MAGNETIC METHOD

2.1 Governing equations & basic theory

Garland [1971] discusses the fundamental equations underlying the magnetic geophysical methods. Various phenomena that require the analysis of magnetic fields occur in a diversity of geophysical situations such as (1) the field of steady and alternating electric currents, (2) the secondary fields engendered from electromagnetic induction in a conductor, and (3) the fields of permanently magnetized (i.e. ferromagnetic) material. Cases 1 and 2 are due to migration of electronic or ionic charges transported under the influence of an applied electric field; while in case 3, the magnetic field originates from the kinetic energy of electrons (namely spin and orbital motion). The governing equations are Maxwell's equations:

$$\begin{aligned} \nabla \times \mathbf{E} &= -\dot{\mathbf{B}} = -\frac{\partial \mathbf{B}}{\partial t}\,; \\ \nabla \times \mathbf{H} &= 4\pi \mathbf{C} + \dot{\mathbf{D}}\,; \\ \nabla \cdot \mathbf{B} &= 0\,; \\ \nabla \cdot \mathbf{D} &= 4\pi\rho\,; \end{aligned} \tag{2.1}$$

where $\mathbf{E}$ and $\mathbf{H}$ are the electric and magnetic field intensities, $\mathbf{D}$ and $\mathbf{B}$ are the electric and magnetic flux densities, $\mathbf{C}$ is the conduction current density, and ρ is the volumetric charge density. These vectors are related to each other by constitutive laws:

$$\mathbf{D} = \epsilon \mathbf{E}, \quad \mathbf{B} = \mu \mathbf{H}, \quad \mathbf{C} = \sigma \mathbf{E} \ , \tag{2.2}$$

where ϵ, μ, σ are the electric permittivity, magnetic permeability, and electrical conductivity respectively.

2.1.1 The main field

The vector magnetic field of the earth is specified by three quantities: (1) magnitude; (2) dip angle above or below a horizontal plane, termed magnetic inclination; and (3) direction with respect to geographic north, termed magnetic declination [Sheriff, 1989]. Details of the current generation geomagnetic reference field (IGRF—11) model can be found in Finlay et al. [2010]. The global scale geomagnetic field, or main field, was determined by Gauss in 1839 [Garland, 1971, 1979] to be largely of internal origin. More recent work indicates that the origin of the main field as well as its secular variation is linked to convective motion of the liquid iron in the outer core [Dormy, 2006]. Additionally, small external contributions to the geomagnetic field with relatively faster variations emanate from geomagnetic storms caused by solar disturbances, and finally; spatial variations of the main field (smaller in magnitude compared to the main field), that are nearly constant in space and time, are generated by permanently magnetized bodies in the crust or near-surface [Telford et al., 1990; Everett, 2013]. The latter are usually the target of geophysical magnetic investigations, as is the case with the work described in this thesis.

The first data processing step is a regional field correction which consists in removing the background magnetic field effect from the total field anomaly (see section 4). In order to understand the background magnetic field, one must understand how the IGRF model is derived, Gauss' original analysis is still used by modern researchers [Garland, 1979]. In his method, the main field is described in terms of a spherical harmonic series, where to each harmonic is assigned an internal and/or external source [Garland, 1971]. At the earth's surface the field $\mathbf{B}(r, \theta, \lambda)$ is described by a scalar potential $U(r, \theta, \lambda)$ satisfying Laplace's equation $\nabla^2 U = 0$ such that $\mathbf{B} = -\nabla U$ where r is the radial distance from earth's center, θ is the polar

angle, and λ is the co-latitude [Garland, 1971; Finlay et al., 2010]. Geophysicists investigate the spatial variations of U over the surface. Laplace's equation $\nabla^2 U = 0$ in spherical coordinates is

$$\frac{\partial}{\partial x}\left(r^2\frac{\partial U}{\partial r}\right) + \frac{1}{\sin^2\theta}\frac{\partial}{\partial\theta}\left(\sin\theta\frac{\partial U}{\partial\theta}\right) + \frac{1}{\sin^2\theta}\frac{\partial^2 U}{\partial\lambda^2} = 0 \ . \tag{2.3}$$

The solution is written as a series of Legendre polynomials with a dependence on distance r. The form of the seres depends whether the source is internal or external to the sphere,

$$\begin{cases} U_e &= a\sum_l^\infty E_l\left(\frac{r}{a}\right)^l P_l^m(\cos\theta) \\ U_i &= a\sum_l^\infty I_l\left(\frac{a}{r}\right)^{l+1} P_l^m(\cos\theta) \end{cases} \tag{2.4}$$

where a is the Earth's radius, U_e is the potential inside or on the sphere caused by an external source, U_i is the potential outside or on the sphere caused by an external source, and E_l is an amplitude factor specifying the contribution of the external source to the lth harmonic, while the term I_l is an amplitude factor specifying the contribution of the internal source to the lth harmonic term. The main field can be approximated by that of a geocentric dipole, such that $m = 0$ it becomes axially symmetric. Hence, for $m = 0$ case the total potential on the earth's surface is:

$$U = a\sum\left[I_l\left(\frac{a}{r}\right)^{l+1} + E_l\left(\frac{a}{r}\right)^l\right]P_l(\cos\theta) \ . \tag{2.5}$$

The geomagnetic field vector $\mathbf{B}_E$ is conventionally described in terms of its elements (X northward; Y eastward; Z downward) and these are obtained by differen-

tiating equation (2.5), resulting in

$$\begin{aligned} X &= \frac{1}{a}\frac{\partial U}{\partial \theta} = \sum \left[E_l \left(\frac{a}{r}\right)^l + I_i \left(\frac{a}{r}\right)^{l+1} \right] \frac{\partial P_l(\cos\theta)}{\partial \theta} \ ; \\ Y &= \frac{1}{a\sin\theta}\frac{\partial U}{\partial \phi} = 0 \ ; \\ Z &= \frac{\partial U}{\partial r} = \sum \left[l E_l \left(\frac{r}{a}\right)^{l-1} - (l-1) I_l \left(\frac{a}{r}\right)^{l+2} \right] P_l(\cos\theta) \ . \end{aligned} \tag{2.6}$$

It is sufficient here to consider the behavior of the $l = 1$ terms involving $P_1(\cos\theta) = \cos\theta$,

$$\begin{aligned} X_1 &= -\left[E_1 + I_1\right] \sin\theta \ ; \\ Z_1 &= \left[E_1 - 2I_1\right] \cos\theta \ . \end{aligned} \tag{2.7}$$

The bracketed terms in equation (2.7) are estimated by fitting observed values of X and Z from geomagnetic observatories distributed worldwide at different latitudes to respectively sine and cosine functions. The unknowns E_1 and I_1 are determined in this way. Extending this analysis to higher harmonics reveals the relative importance of the internal and external sources. Gauss, in his analysis of a limited number of measurements, applied the above method to only the $l = 0$ term [Garland, 1971]. He concluded that almost all of the main field is generated by internal sources [Garland, 1971]. With higher computing power of modern technology and much more extensive magnetic databases, scientists are now able to analyze the first few harmonics with great precision; notwithstanding, Gauss's conclusion remains unchanged, that an internal dipole described by P_1^0 is strongly dominant.

The horizontal intensity of the geomagnetic field is given by $H = (X^2+Y^2)^{1/2}$ and the total intensity is $F = (X^2+Y^2+Z^2)^{1/2} = |\mathbf{B}_E|$. The geomagnetic dip, also termed inclination I, is the vertical angle between the geomagnetic field direction and the horizontal plane, $I = \tan^{-1}(Z/H)$. The declination D of the magnetic meridian, the

vertical plane containing the geomagnetic field vector, is given by $D = \sin^{-1}(Y/H)$ [Blakely, 1995; Kearey, 2002]. The geomagnetic field elements are shown in Figure 2.1 and maps of declination D, inclination I, and total field intensity F from the current IGRF model are shown in Figure 2.2.

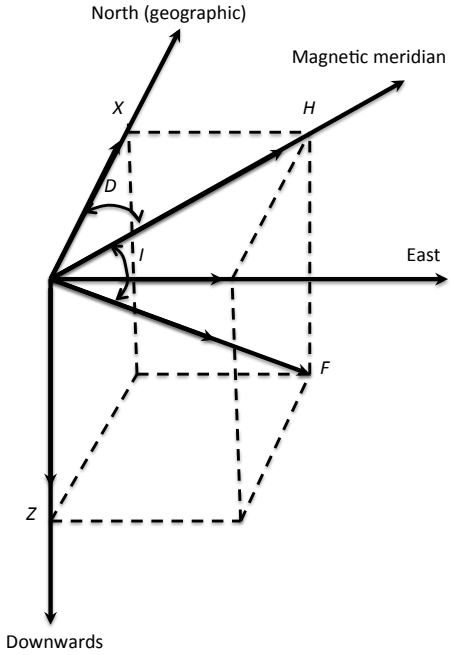

FIG. 2.1. Geometry of the total field intensity F, horizontal component H, vertical component Z, inclination I, and declination D [from Kearey, 2002].

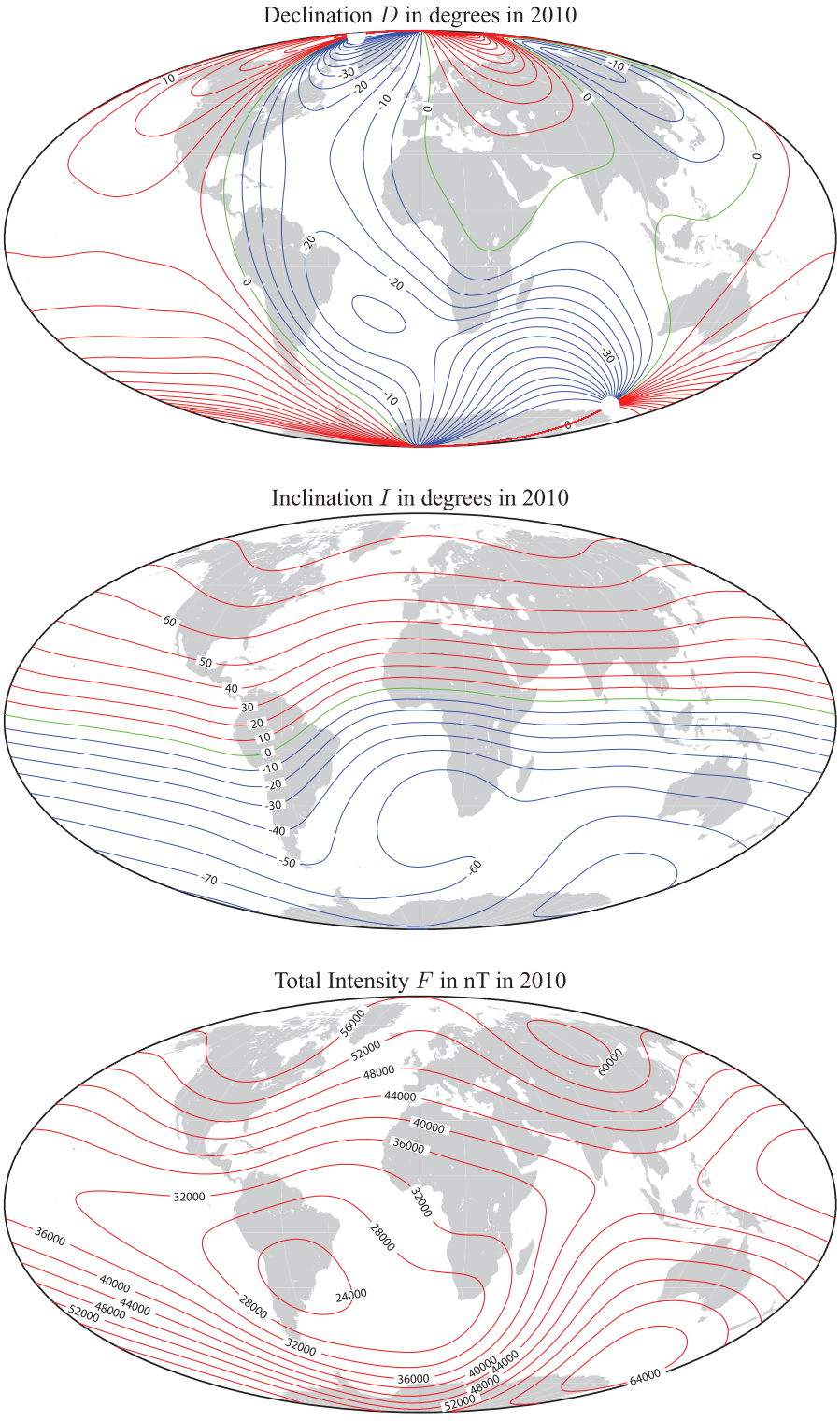

FIG. 2.2. Maps of the IGRF—11 model. (top) Declination D in degrees; (middle) inclination I in degrees; and (bottom) total field intensity F in nT [from Finlay et al., 2010].

2.1.2 Theory

In this section, basic theory of the magnetic geophysical method is described summarizing Sharma [1997] derivation. The scalar magnetic potential W at an observation point P due to a pole of strength p located at some distance r is given by:

$$W(P) = \frac{\mu_o}{4\pi}\left(\frac{p}{r}\right) \tag{2.8}$$

where μ_o is the magnetic permeability of free space, measured in Henrys per meter [H/m] in SI units. Its numerical value is $4\pi \times 10^{-7}$ H/m. The negative gradient of the potential (equation 2.8), yields the magnetic flux density $\mathbf{B}$, which is oriented in the direction of r at point P and given by

$$\mathbf{B} = -\text{grad}\, W = \frac{\mu_o}{4\pi}\left(\frac{p}{r^2}\right)\mathbf{r}_1 \tag{2.9}$$

where $\mathbf{r}_1$ is the unit vector oriented from the magnetic pole towards point P. The sign convention defines the north-seeking pole as positive. The pole strength p is measured in Ampere-meters (Am), distance r in meters (m), and the flux density $\mathbf{B}$ in Teslas (T). Electric currents also produce a magnetic field, which can be described in terms of the forces that curl around the electric currents. The field produced by electric currents is called the magnetizing field $\mathbf{H}$. The SI unit of $\mathbf{H}$ is Ampere per meter (A/m). The magnetizing field strength due to current i at distance r is $\mathbf{H} = (i/2r)\hat{\phi}$ where $\hat{\phi}$ is the azimutal direction circulationg around the current i. The relationship between $\mathbf{B}$ and $\mathbf{H}$ is shown in equation (2.2). A magnetic material may be considered as a set of infinitesimal current loops (dipoles) whose axes are oriented in the direction of magnetization J measured in A/m. For instance, a bar magnet can be considered as an assemblage of many elementary dipoles oriented along its

axis (see Figure 2.3).

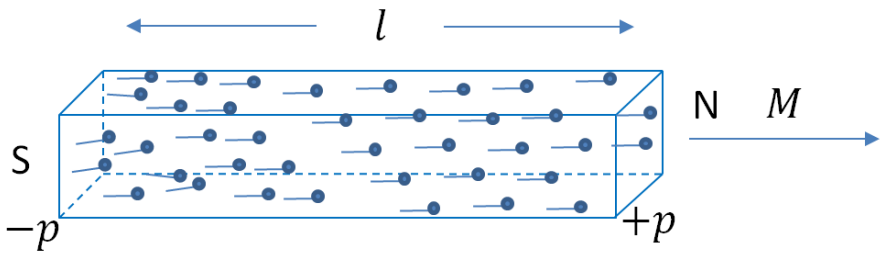

FIG. 2.3. Illustration of a uniformly magnetized bar as a set of infinitesimal current loops (dipoles). The intensity or strength of magnetization can be expressed in terms of pole strength, p, or magnetic moment, **M** [Sharma, 1997]

.

The magnetic intensities of the elementary dipoles inside the bar volume cancel out one another with exception of the dipoles located at the end faces. Hence, the magnetized bar will have positive (N) pole and negative (S) pole of strength $+p$ and $-p$ at each end, respectively.

$$\mathbf{J} = \left(\frac{p}{A}\right)\mathbf{r}_1 \qquad [\mathrm{A/m}] \tag{2.10}$$

where A is the area of the end faces, and $\mathbf{r}_1$ is a unit vector that extends from the negative toward the positive pole. The magnetic moment M can be defined as:

$$\mathbf{M} = (pl)\,\mathbf{r}_1 = p\mathbf{r}_1\left(\frac{V}{A}\right) = JV\hat{\mathbf{r}} \qquad [\mathrm{A}m^2] \tag{2.11}$$

where V is the volume of the bar magnet. Equation (2.11) is relevant because a magnetic body of any shape possesses a volume V and magnetization J. A fault or a lithologic contact can be approximated to a line of point dipoles.

2.2 Magnetic petrology

The concept of magnetic petrology [Clark, 1997] integrates conventional and rock magnetism petrology to describe, abundance, composition, processes that create, alter and destroy magnetic minerals in rocks. Understanding the magnetic mineralogy of rocks and its properties can result in improved geological interpretation of magnetic survey. Rocks and or minerals composed of ferrous and ferric iron content (i.e. magnetite, hematite, amphibolites, granites) exhibit abnormal magnetic signature than its surround [Clark, 1997]. Geology of the study area discussed in section 1.3 presents an abundance of magnetic minerals that contribute to the anomalous magnetic readings. Figure 2.4 shows X–ray diffraction performed on a Hematitic sandstone sample from the study site.

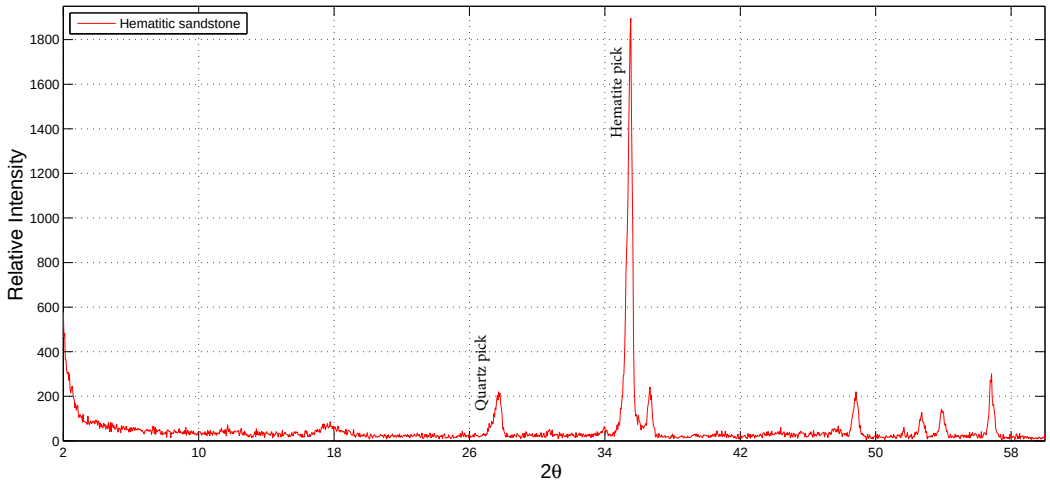

FIG. 2.4. XRD analyze of a Hematitic sandstone sample collected near 80 m along line 1. The Quartz (SiO_2) and Hematite ($Fe_2^{3+}O_3$) picks are indicated on the plot.

2.3 Field equipment

Magnetic data can be acquired in land, air, sea, or via satellite. Although magnetic data for this thesis was acquired using a Cesium vapor magnetometer, the most common instruments are the fluxgate and proton-procession magnetometers. Many instruments designed in the early 1900s were capable of measuring the geomagnetic elements Z, H and the main field **B**. The precision is normally ± 0.1 nT [Kearey, 2002]. The instrument used to acquire the data presented in this thesis is the Geometric—G858 Cesium Vapor magnetometer which measures intensity of magnetic field $|\mathbf{B}|$ (Figure 2.5 the instrument consists of both the console, at left, and the sensors, at right). A detailed description of the principle of operation of the Cesium Vapor magnetometer can be found in Everett [2013].

FIG. 2.5. (left) Geometric—G858 Cesium vapor magnetometer console. (right) Deployed equipment in the field using two sensors (lower B2 at 0.6 m and upper B1 at 1.6 m above the ground).

3. DATA ACQUISITION

A Geometric-G858 Cesium vapor magnetometer instrument (Figure 2.5) was used to acquire the data. The station spacing was set to 0.5 m, base station readings were made after reading every 20 m, and line spacing set to 5 m, rendering a total of 19 N-S lines of 150 m each covering $95 \times 150\ m^2$ and one E-W line of 200 m length. The first two lines where acquired on October 6-7, 2012, each with station spacing at 0.1 m, and with a base station reading after every 20 m. The next two were acquired using 0.4 m station spacing, base station at every 20 m and 150 m profile length. The remaining lines were acquired on November 2, 2012 with the same parameters as the previous two except each station readings were made every 0.5 m. Figure 3.1 shows the layout of the survey lines.

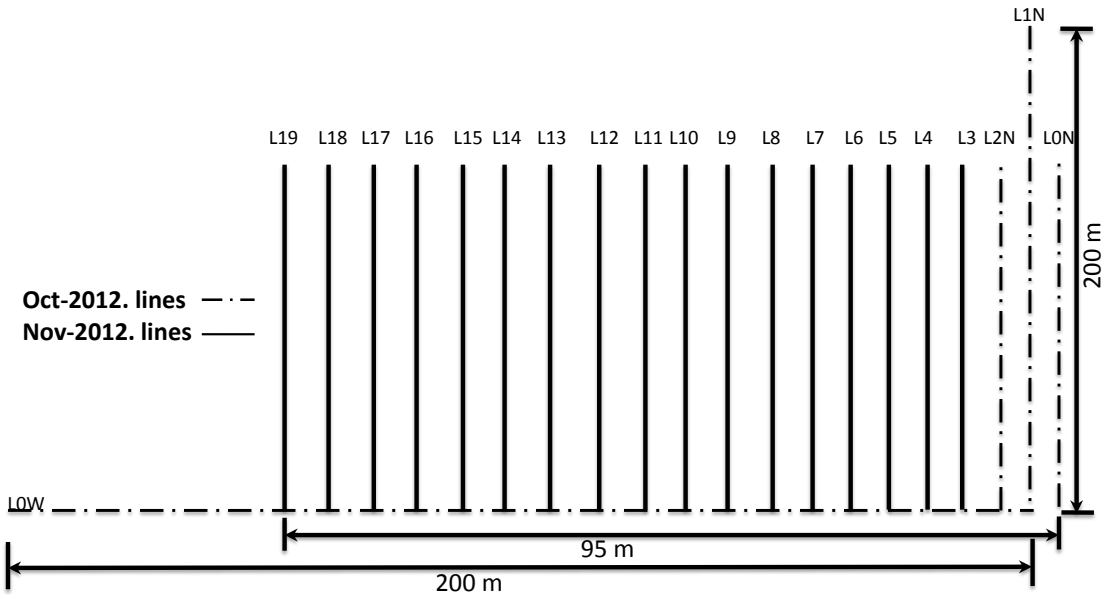

FIG. 3.1. Schematic of the survey. Line 0W was acquired in the E-W direction and lines 0 to 19 were acquired in the N-S direction.

Two sensors separated by $1\,m$ were used to collect vertical gradiometry data. Gradiometry measurement is the difference between the magnetic field $\mathbf{B}_i$ recorded at the i-th sensor position and the magnetic field $\mathbf{B}_j$ recorded at the j-th sensor position [Everett, 2013]. In contrast to single magnetometer measurements, gradiometry data reveals finer details regarding the spatial variation of the subsurface magnetized bodies [Everett, 2013]. In this work, the lower sensor was positioned at $0.6\,m$ and the upper at $1.6\,m$ from the ground.

Daily solar indices can be found at `www.swpc.noaa.gov/ftpmenu/indices/old_indices.html`. The data summarizes daily solar indices collected every three hours beginning at 0030 UTC. These indeces indicate whether a particular day is suitable for magnetic survey $K < 5$ or not $K \geq 5$. The closest observatory to Mason Texas is the Fredericksburg's (see Table 3.1).

Table 3.1. K-indices data from Fredericksburg's observatory. These indices indicate quiet days suitable for magnetic survey ($K < 5$) and noise days unsuitable for magnetic survey ($K \geq 5$).

Date	K-indices
Oct 06, 2012	2 1 1 2 2 2 1 1
Oct 07, 2012	0 2 1 2 1 1 1 2
Nov 03, 2012	0 0 0 0 2 1 1 0

4. DATA PROCESSING AND INTERPRETATION

4.1 Diurnal correction & line leveling

Magnetic data processing steps are fairly straightforward. Diurnal correction is performed to account for temporal variation in the geomagnetic field due to solar activities in a period less than a day. The base station readings were used to correct for temporal variation. After diurnal correction, line leveling was performed to eliminate non-geological effects caused by long wavelength noise in the survey direction [this correction followed the steps outlined in the Geosoft technical note by Whitehead, 2004].

4.2 Regional correction

A total field instrument such as the cesium vapor magnetometer, measures the strength of the magnetic field $|\mathbf{B}_{OBS}|$ due to all sources present around the observation point. Therefore, the observed field intensity is $|\mathbf{B}_{OBS}| = |\mathbf{B}_E + \mathbf{B}_T|$ where $\mathbf{B}_E$ is the ambient geomagnetic field and $\mathbf{B}_T$ is the target field. To reveal the magnetic anomaly $\mathbf{B}_T$ due to the buried or localized source, it is necessary to remove the background geomagnetic field intensity $\mathbf{B}_E = \mathrm{F}$. The total-field anomaly T is defined as

$$\mathrm{T} = |\mathbf{B}_{OBS}| - \mathrm{F} \tag{4.1}$$

Equation (4.1) can be viewed as the combination of the instrument reading $|\mathbf{B}_{OBS}|$ taken in the field and the chart reading F (background anomaly) from the current IGRF geomagnetic field model. An online calculator that produces values of F based on IGRF—11 is available at `www.ngdc.noaa.gov/seg/geomag/magfield.shtml`. Using the calculator above mentioned, the ambient geomagnetic field strength

at Mason is 48,005 nT, with $59^o27'$ inclination, and declination $5^o11'$. On the acquisition date (Nov. 3, 2012), the north and east component of the magnetic field are 24,302 and 2,204.8 nT respectively (see Figure 4.1).

Lat: 30° 45' 6" Lon: - 99° 13' 57" Elev: 0.00 m	Declination + East - West	Inclination + Down - Up	Horizontal Intensity	North Component + North - South	East Component + East - West	Vertical Component + Down - Up	Total Field
11/3/2012	5° 11'	59° 27'	24,401.8 nT	24,302.0 nT	2204.8 nT	41,340.2 nT	48,004.8 nT
Change per year	- 8' per year	- 2' per year	-28.0 nT/year	-22.9 nT/year	-57.4 nT/year	-106.6 nT/year	-106.0 nT/year

FIG. 4.1. Results from the IGRF—11 calculator. Location Mason TX, date Nov. 3, 2012.

4.3 Reduction to pole filter

A number of processing steps should be performed before interpreting the data. In conventional practice, magnetic data reduction includes the removal of any regional field effect by subtracting from each measured value an average of the total magnetic intensity over the surveyed area. A regional field is one whose characteristic spatial variations are longer than the characteristic size of the survey area. Reduction to pole filtering (RTP) is a technique that transforms the data from that actually acquired in the presence of the inclined ambient geomagnetic to the data that would have been acquired in the presence of a vertical magnetizing field at inclination 90^o [Milligan and Gunn, 1997], as found at the north geomagnetic pole. The purpose of the RTP filter is therefore to remove distorting effects due to the inclination of the magnetizing geomagnetic field. Mathematical derivation of the RTP filter can be found in Everett [2013]. An illustration of the effect of the RTP filter along one of the survey profiles is shown in Figure 4.2. Maps of the original and RTP-filtered total field anomaly data after regional correction, are shown in Figure 4.3 for the top sensor.

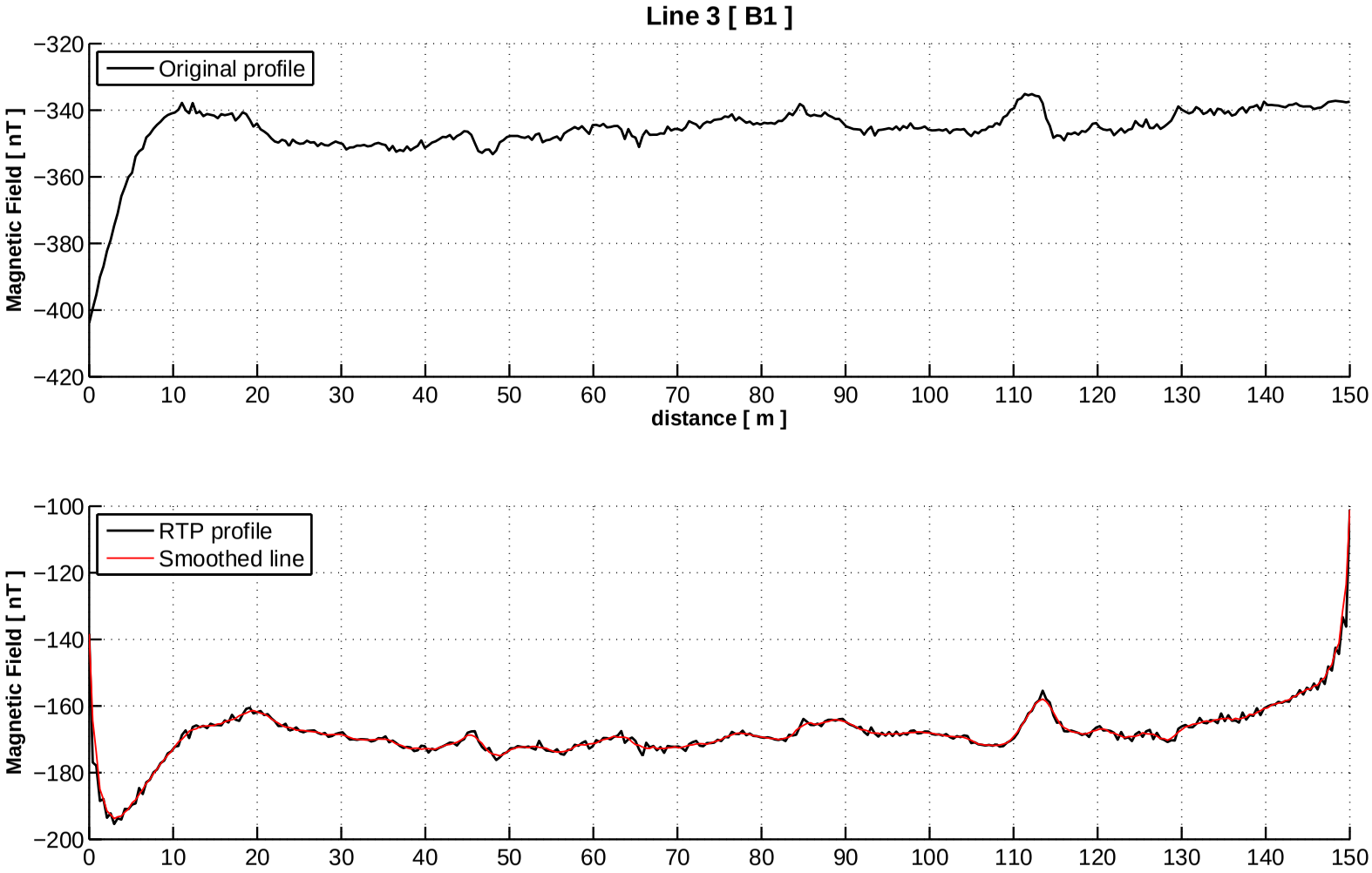

FIG. 4.2. Original (top) and RTP-filtered (bottom) profiles along line 3.

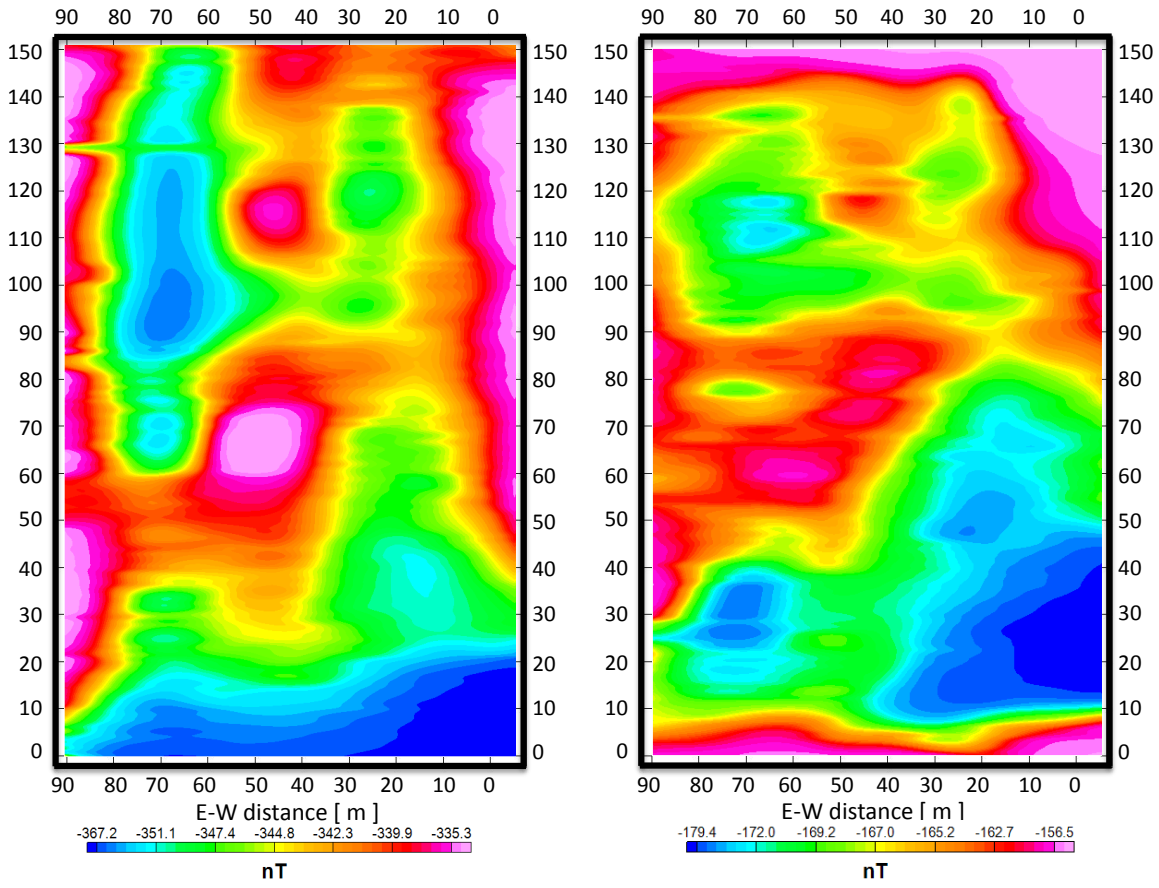

FIG. 4.3. Original (left) and RTP-filtered (right) maps of the study area. The RTP-filter was applied to the data following a regional field correction. Top (B1) sensor is being mapped.

4.4 Euler deconvolution

Depths to magnetic sources are estimated using Euler deconvolution. This processing step can be applied to either single-profile [Thompson, 1982] or gridded [Reid et al., 1990] magnetic anomaly data. The technique is based on the Euler homogeneity equation [Thompson, 1982]:

$$x\frac{\partial f}{\partial x} + y\frac{\partial f}{\partial y} + z\frac{\partial f}{\partial z} = nf \tag{4.2}$$

or in vector notation [Blakely, 1995, p.243]

$$r \cdot \nabla f = -nf \tag{4.3}$$

where n is the degree of homogeneity

Many magnetic sources at depth generate an anomalous magnetic field of the form:

$$f(x, y, z) = \frac{G}{r^N} \tag{4.4}$$

where $r = (x^2 + y^2 + z^2)^{1/2}$, and $N = 1, 2, 3, ...$ The parameter G does not depend on x, y, or z; therefore, equation (4.4) is homogeneous of degree $n = -N$. In this work, depth estimation was made using the Euler software written by Cooper [2004] for the profile data and the standard Euler deconvolution from the Oasis montaj [Geosoft, 2012] package for gridded data. The structural indices N of different magnetic sources are given in Table 4.1. The application of Euler deconvolution to RTP-filetered data produces better depth estimation [Reid et al., 1990] than deconvolution of the corresponding unfiltered data. Examples of Euler deconvolution are shown in Figures 4.4 and 4.5 for profile data. It is important to note that the source location $Q(x', y', z')$ is referenced to the observation point $P(x, y, z)$ so that the Laplace's equation is rewritten $(x - x')\frac{\partial U}{\partial x} + (y - y')\frac{\partial U}{\partial y} + (z - z')\frac{\partial U}{\partial z} + NU = 0$ [Everett, 2013].

Figure 4.6 shows the Euler deconvolution solutions plotted over the RTP map (left) and the solutions only (right). The structural index $N = 1$ is mapped. Due to steeply deeping beds and rocks with high magnetic susceptibility near the surface within the study area, Euler deconvolution solutions at $N = 1$ shows the fault contact starting at $y = 100$ m. Structural indices between 0 and 1 reveal contacts and faults. Euler deconvolution solutions from $N = 0.7$ to 2 are shown in Figure 4.7.

Table 4.1. Structural indices for magnetic data [after Durrheim and Cooper, 1998 and Everett, 2013].

model	causative body	structural index, N
none	fault	1
line of poles	semi-infinite sheet	1
poles	finite sheet	2
line of dipoles	semi-infinite thin dike	2
Point dipole	finite thin dike	3

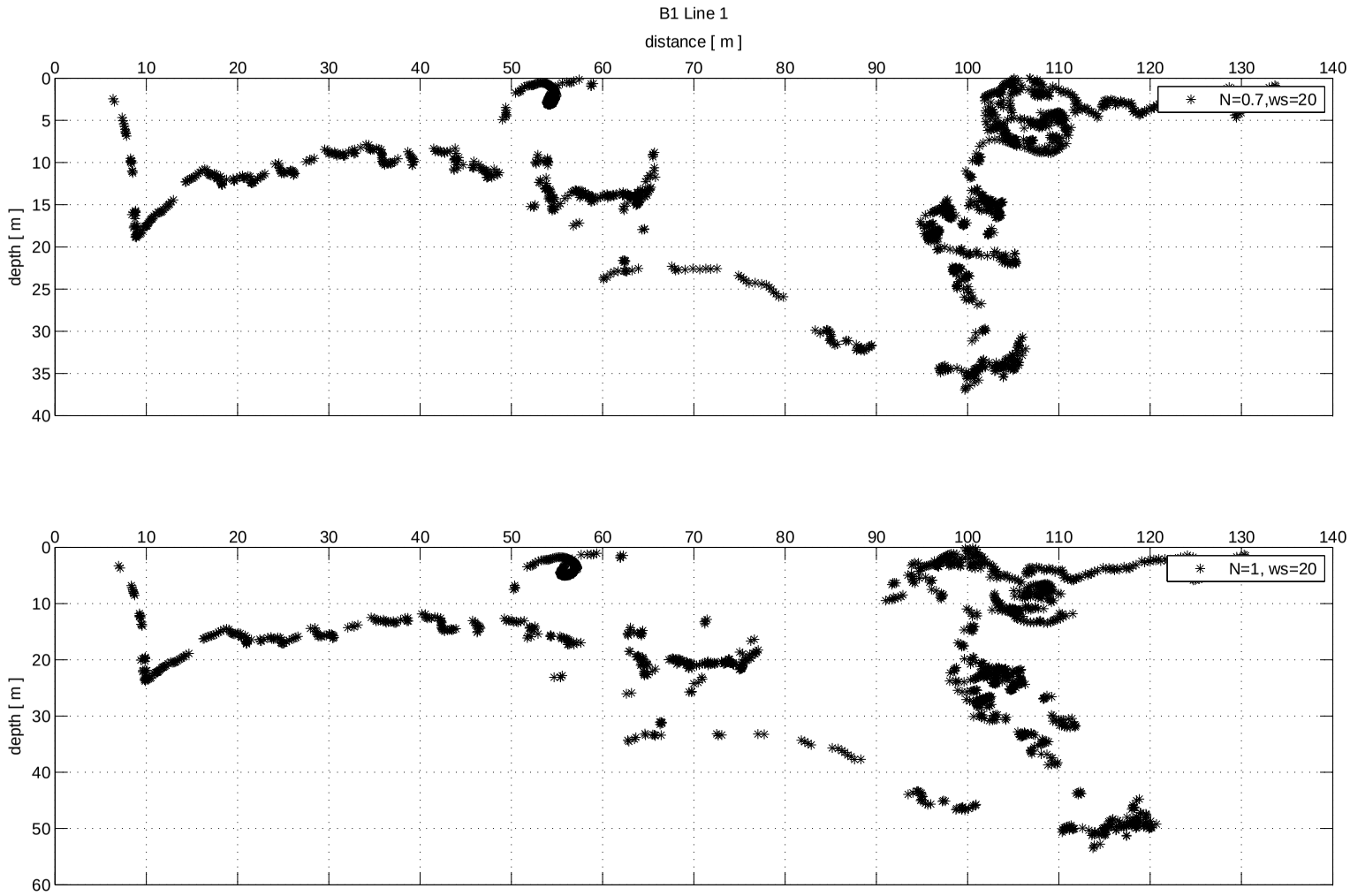

FIG. 4.4. B1 Euler deconvolution solutions along line 1, center of the N-S road. Top $N = 0.7$ and bottom $N = 1$.

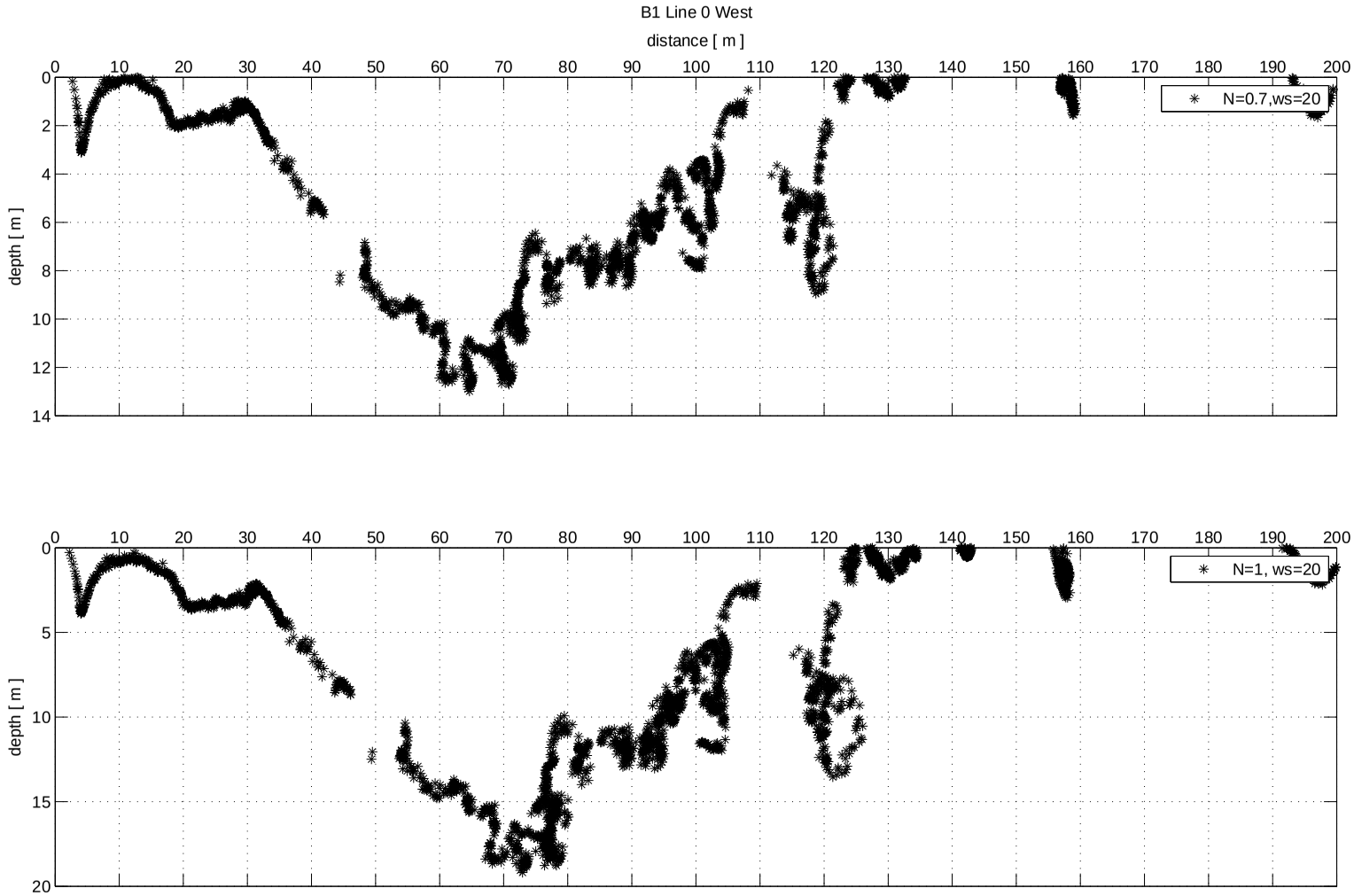

FIG. 4.5. B1 Euler deconvolution solutions along line 0W, center of the E-W road. Top $N = 0.7$ and bottom $N = 1$. The sources of magnetic anomaly are shallower than those of the N-S lines.

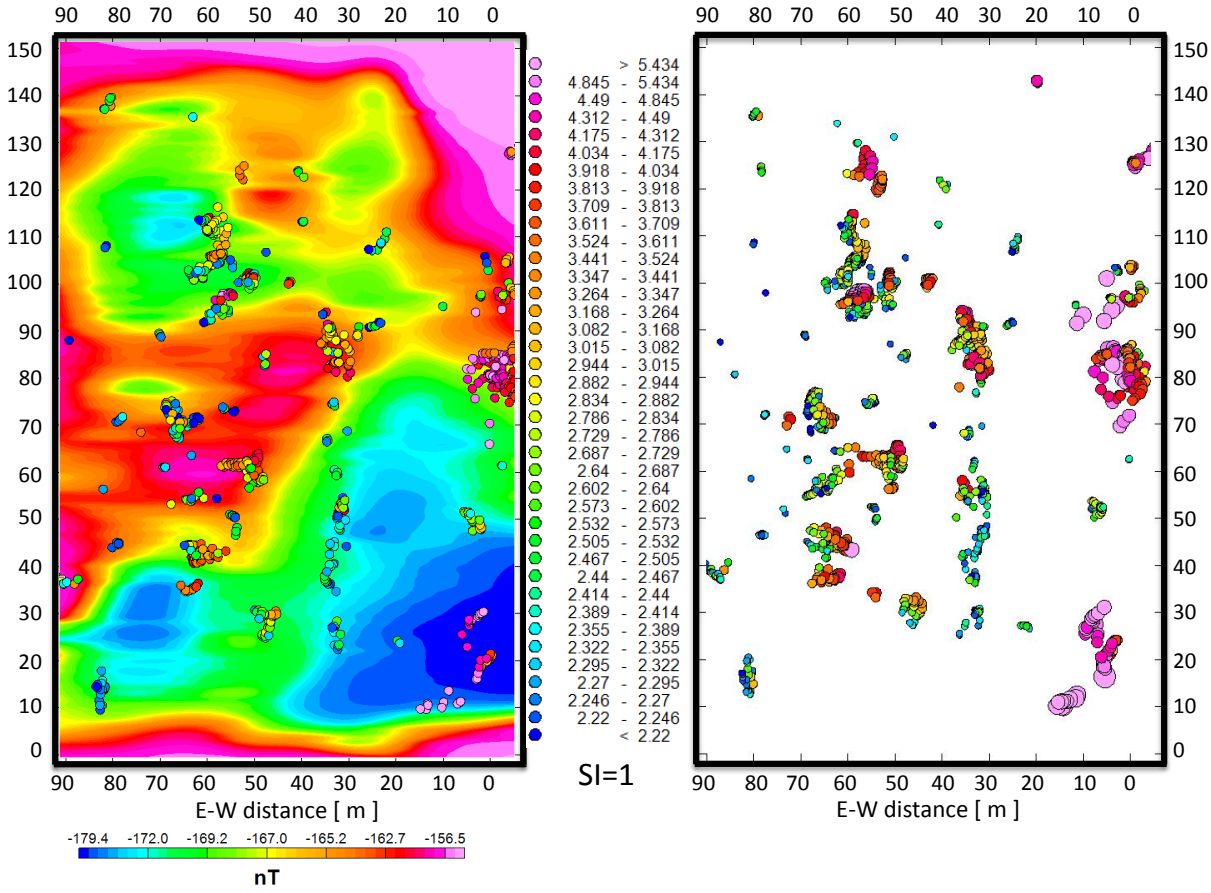

FIG. 4.6. (left) RTP map overlain by the Euler deconvolution solutions at structural index $N = 1$, and computational window size of 15. (right) Euler deconvolution solutions without the RTP map in the background.

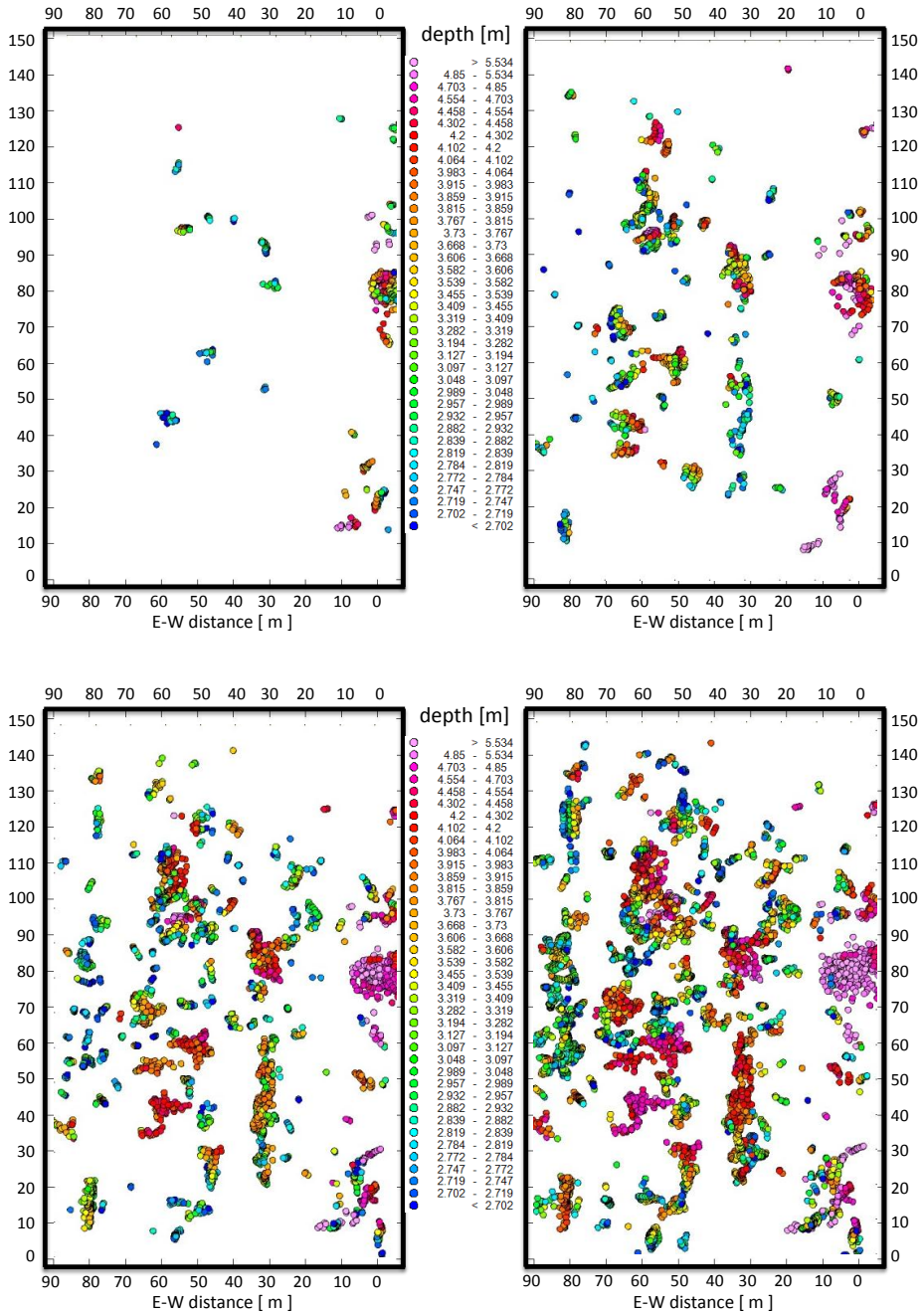

FIG. 4.7. Euler deconvolution solutions for several structural indices. Top left $N = 0.5$, top right $N = 1$, bottom left $N = 1.5$, and bottom right $N = 2$.

4.5 Inversion & forward modeling

4.5.1 Inversion

Quantitative estimation of the geometric and material parameters of a buried magnetic source is a geophysical inverse problem [Tontini et al., 2006]. The goal of inversion is to convert the observed magnetic data into a model of the subsurface magnetization that reveals the source of the magnetic signal. The acquired profile data have been used to generate subsurface magnetization models of the study area. The subsurface models are generated using data from both top (B1) and bottom (B2) sensor data. Vertical cross-sections for individual lines of magnetization $M(x, z)$ are produced. An example of inversion cross-section is shown in Figure 4.8. Euler deconvolution plotted over the inversion result is shown in figure 4.9 in which the fault seem to be dipping $\sim 70^o$ NW.

4.5.2 Forward modeling

In order to understand the magnetic signature of different faults, Grauch et al. [2000] shows the magnetic response of using four simple models, (a) truncated-layer model, (b) offset-layer model, (c) thin-thick layers model, and (d) disparate layers models see Figure 4.10. In general, the depth to the source of a magnetic anomaly can also be obtained using the half-width $x_{1/2}$ of the anomaly [Sharma, 1997]. Mathematical depth (Table 4.2) rules can be derived for different subsurface geometries which lead to a better interpretation of potential field data.

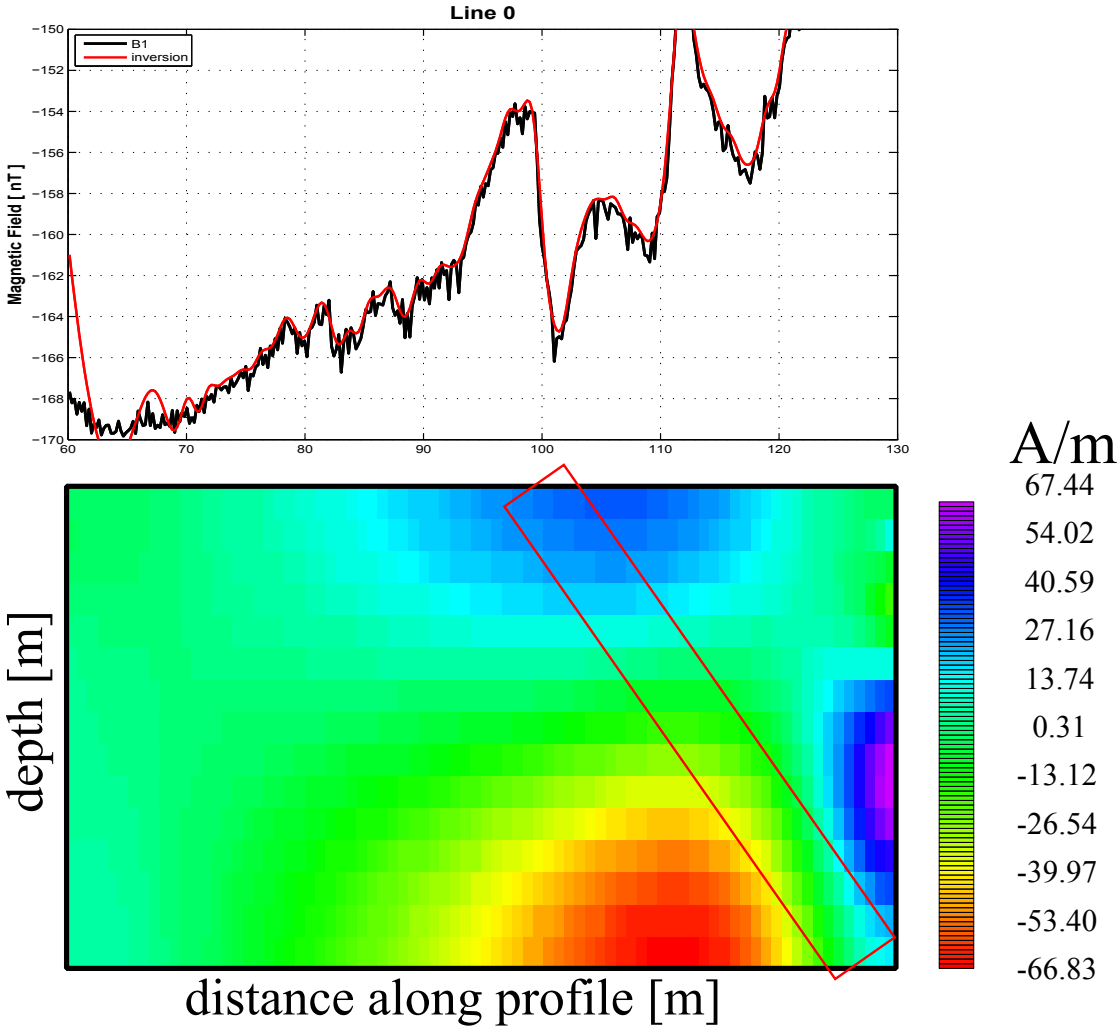

FIG. 4.8. Inversion of line 0. (top) 2D inversion of the RTP-filtered data of sensor B1. The input data is shown in black while the model response is shown in red. (bottom) The inversion was performed using a model discretization of 15×80 cells. Magnetic susceptibility κ is being plotted. The red rectangle indicates the approximate location of the fault.

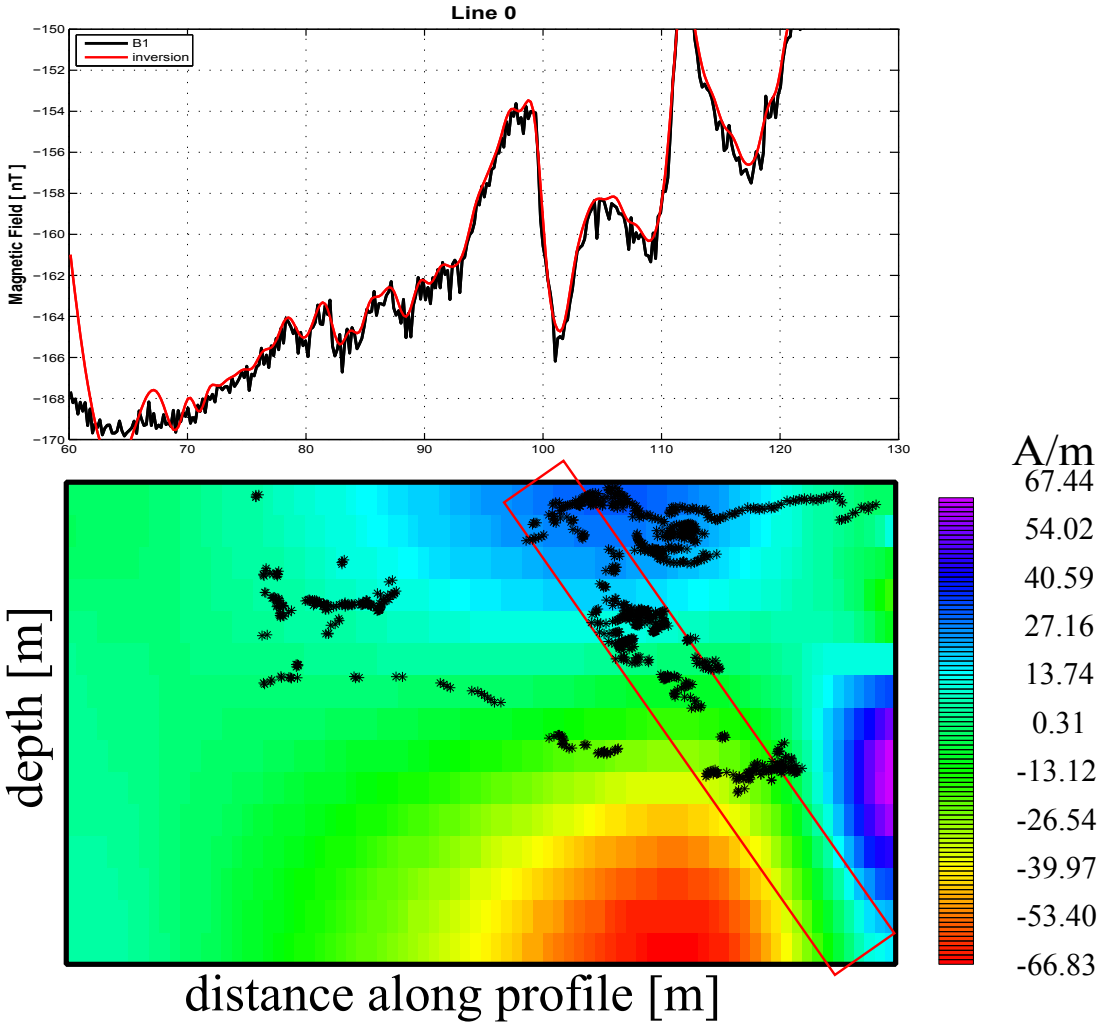

FIG. 4.9. Inversion of line 0. (top) 2D inversion of the RTP-filtered data of sensor B1. The input data is shown in black while the model response is shown in red. (bottom) Inversion image superimposed by Euler deconvolution solutions using SI = 1 and window size 20. Magnetic susceptibility κ is being plotted. The red rectangle indicates the approximate location of the fault dipping $\sim 70^o$ NW.

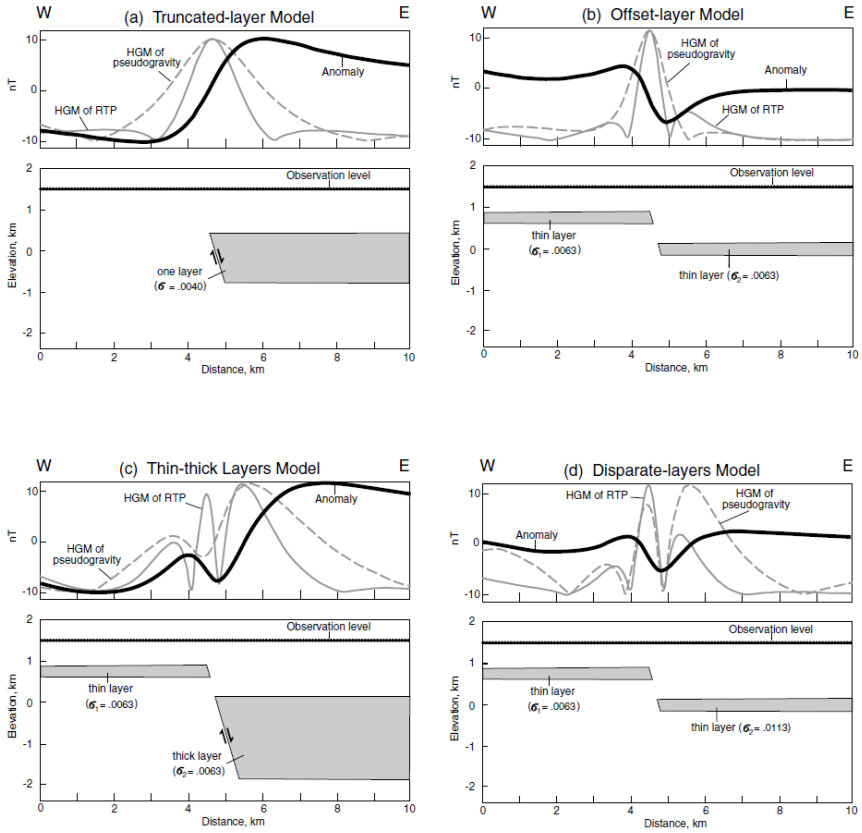

FIG. 4.10. Forward models showing the aeromagnetic signature of faults typically. Magnetic anomaly is shown in bold black line, the horizontal-gradient of the RTP filtered data is show in solid gray line and pseudogravity (synthetic gravity generated from magnetic data) in dashed gray line. (a) Truncated-layer model is similar to a fault-contact model. (b) The offset-layer model contains a displaced layer along the fault. (c) The thin-thick layers model has a downthrown layer that is much thicker than the upthrown layer, and (d) the disparate-layers model has two offset that have equal thicknesses but different magnetizations [after Grauch et al., 2000].

Table 4.2. Magnetic anomaly formulas and depth rules for simplified sources with vertical magnetization. $\triangle Z$ is the vertical magnetic component in nT, $c = 100$, x is the horizontal distance along the profile, $\triangle J_z$ is the magnetization contrast in [A/m] computed from $J = \kappa(F/\mu)$, z is the depth to the center of the magnetic body, z_1 and z_2 are depths to the top and bottom of the body, respectively, and $x_{1/2}$ is the half-width of the magnetic anomaly [modified from Sharma, 1997].

Source(tabular model)	Magnetic anomaly ($\triangle Z$)	Depth rule
Vertical fault	$\triangle Z = 2c\triangle J_z - \tan\left\|\frac{\pi}{2} - \tan^{-1}\left(\frac{x}{z}\right)\right\|_{z_1}^{z_2}$	$\triangle Z = 2x_{1/2}$
Vertical contact	$\triangle Z = 2c\pi\triangle J_z$	

Forward modeling is an excerse of trial and error in which the investigator builds a subsurface model that fits the observed data. The model needs to be consistent with what is known about the geology. Upon adjusting all the parameters that account for subsurface geology, the ideal model will closely match the observed data.

Some vertical faults and contact scenarios were modeled to match the response of the fault the study area. Sharma [1997] discusses the magnetic signature of a vertical fault Figure (4.11). Six model scenarios are presented in Figure 4.12. By comparison with the RTP-filtered data, the most likely scenario is the model (e) because it shows a slight dip curvature on the magnetic response that can be equated to the one seen on profile data (see Figure 4.2 at $x = 105$ m). The model contains a small gap and an offset, two different susceptibility contrast to resemble the Hickory sandstone (blue) and the granite (red). This gap may be consistent with either open or fill fractures within the fault zone, thus, the placement of Euler solutions (Figure 4.4) cluster at $x = 100 - 105$ m.

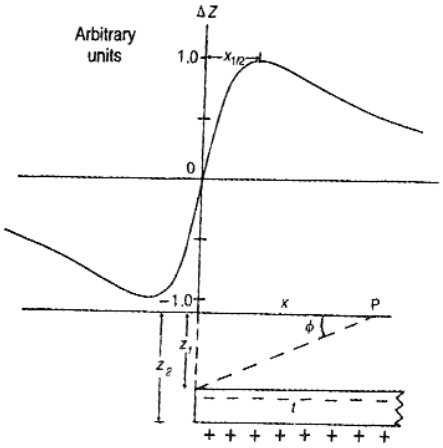

FIG. 4.11. Magnetic signature of a vertical fault $\triangle Z = B_z$. The gradient of the anomaly is highest over the edge of the fault. The half-width $x_{1/2}$ of the anomaly is used as an indicator of depth [Sharma, 1997]

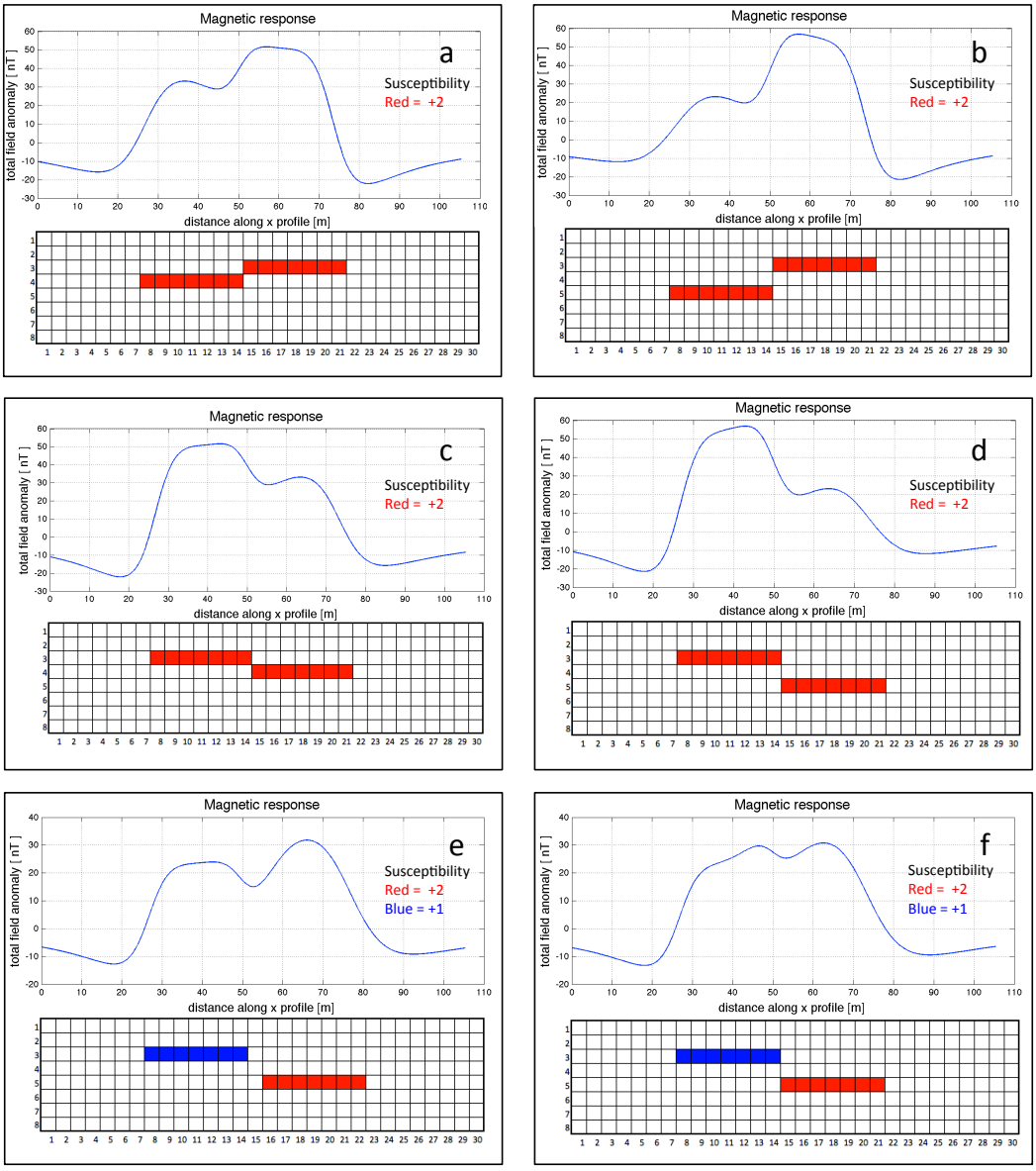

FIG. 4.12. Models with their respective magnetic response. The models were constructed using 30×8 cells with the lithogy (red and blue) ocupying 7 cell on either side of the fault. (a) Geologic model of a vertical fault representing one medium offset by the fault. The magnetic susceptibility value is 2, the layer closer to the surface has higher magnetic response. (b) Similar scenario as b except a greater throw has been introduced. (c) and (d) represent the same scenario as the previous two except the layers have been revrsed. (e) A lower magnectic susceptibility have been introduced to resemble the WMA scenario. A larger fault separation is introduced to represent filled or open fractures withing the fault zone. (f) The fault separation from (e) is removed, showing less magnetic variation.

5. RESULTS & DISCUSSION

5.1 Magnetic method results compared to GPR

GPR data acquired along the N-S road (equivalent to magnetic line 1) is shown in Figure 5.1. Readings were recorded at every .1 m along 150 m profile. The red circle indicates strong reflection associated with the fault at approximately $x = 97$ m. In the magnetic data, the fault is located at $x = 100$ m. Both methods are also in agreement as to the location of the fence at the left end and the granitic basement rocks at the right end side of the profile.

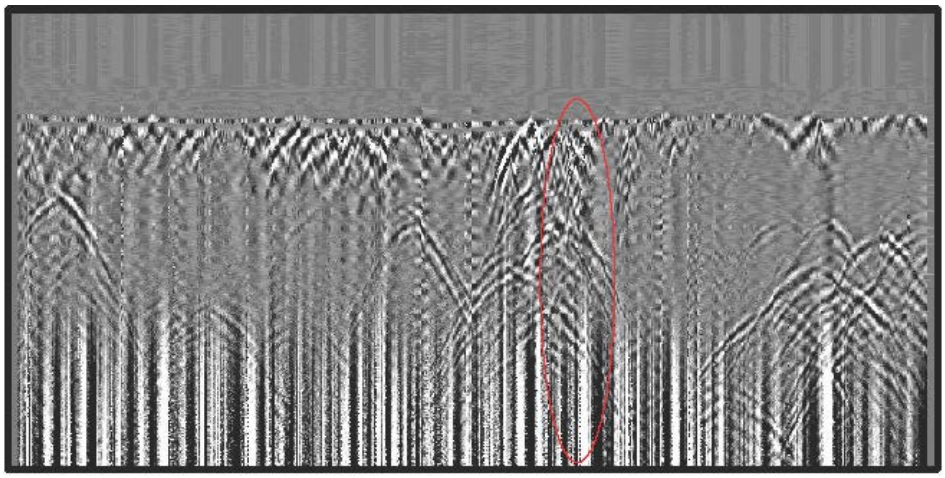

FIG. 5.1. GPR data acquired on the same profile as magnetic survey line 1. The total profile length is 150 m. Red circle indicates the fault location.

5.2 Magnetic method results compared to EM

Murphy [2014] is currently investigating the EM response of the target fault of this thesis. The instrument in use is the Geonics EM TEM47. EM data was acquire along N-S road (equivalent to line 1 of the magnetic method), reading were taken at every 2 m with receiver and transmitter separation of 18 m along 150 m profile. Preliminary results indicate that anomalous dips at 52 and 100 m separation which may be associated with the targeted fault (see Figure 5.2). Magnetic data collected along the same profile as EM shows the fault location at approximately $x = 100$ m.

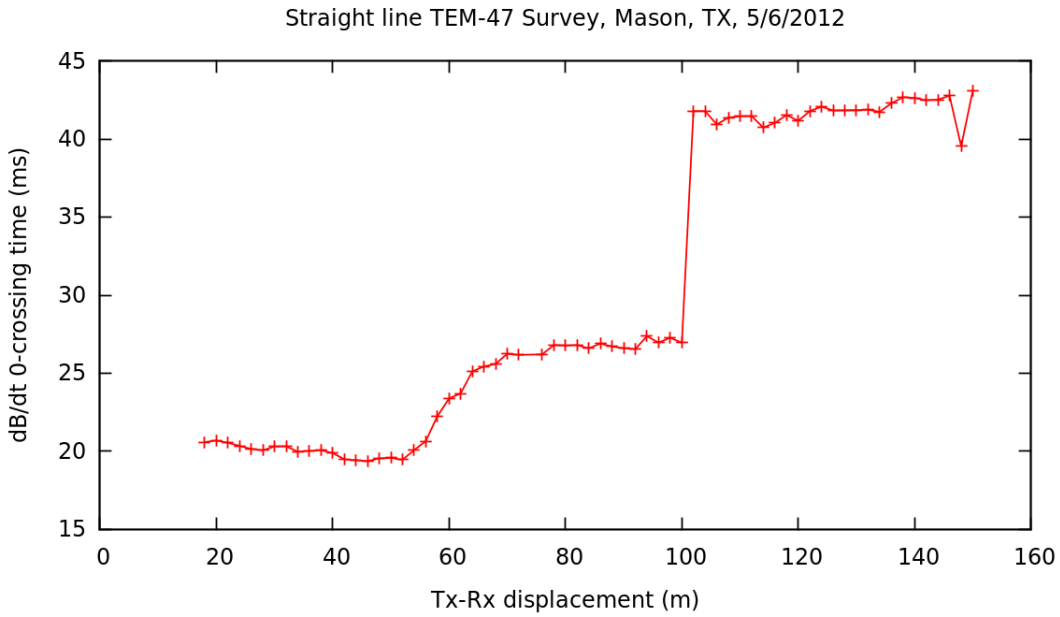

FIG. 5.2. EM 0—crossing results along N-S road. [after Murphy, 2014]

5.3 Magnetic method results compared to seismoelectric

Cohrs [2012] conducted an extensive investigation using both seismic and seismoelectric geophysical methods. Seismoelectric method calibrated by standard seismic reflection, was utilized to image a fault zone with fault-trapped P-wave. Both magnetic and seismoelectric targeted the same fault but at different locations. The survey layout for the seismoelectric experiment consisted of three zones based on lithology; (1) the Pre-Cambrian granite zone, (2) the fault zone, and (3) the Hickory sandstone zone. Cohrs [2012] observed that only the fault zone presented late wave arrivals which were consistent with fault-trapped guided waves (see Figure 5.3). Similarly, the magnetic method presents high magnetic anomaly at the fault location. Figure 5.4 shows the magnetic map of the lower sensor and the profile along line 1. The fault is located at $x = 98$ m.

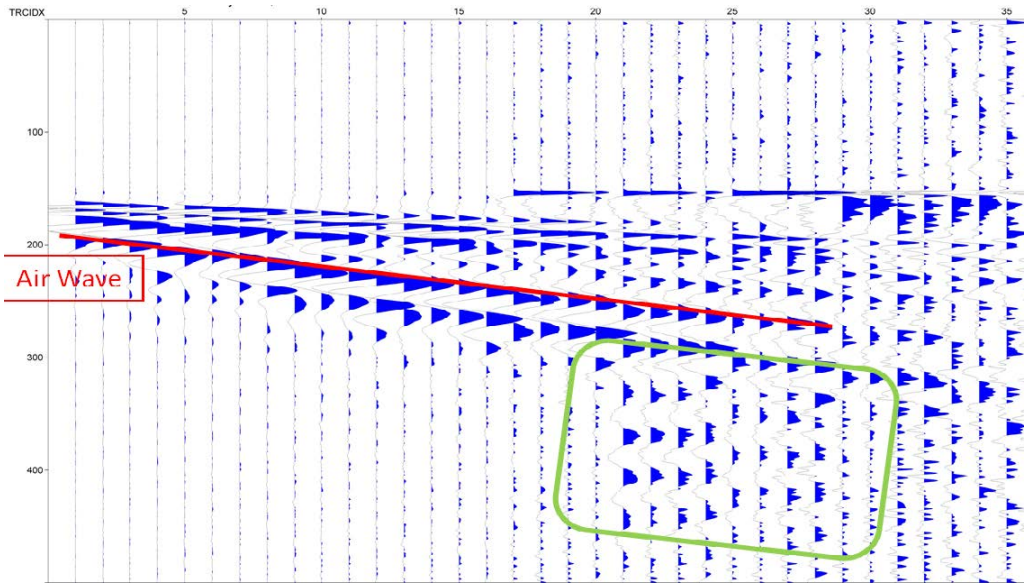

FIG. 5.3. Siemoelectric shot collected in the fault zone. Air wave propagation is marked by the red line. The target zone of interest is distinguishable by late-arriving high amplitude signal. [from Cohrs, 2012]

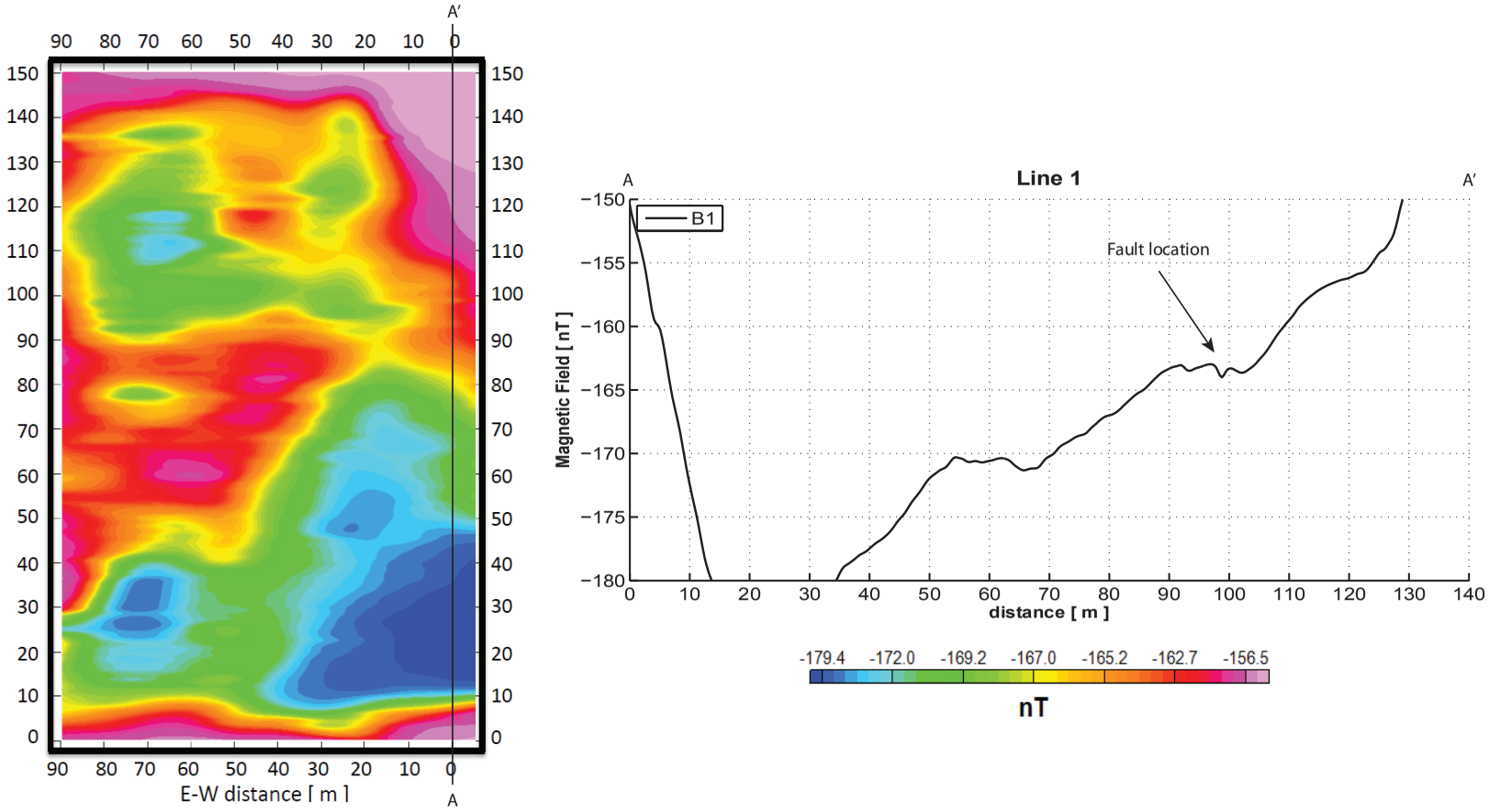

FIG. 5.4. (left) Map of the total magnetic intensity B1. (right) Profile along line 1, from A to A' showing the fault location.

6. SUMMARY & CONCLUSION

In summary, a magnetic study over a 95×150 area at MMWMA was carried out as part of multitechnique geophysical investigation that includes GPR, EM, seismic and seimoelectric surveys. Elementary processing steps were employed to characterize a faulted zone. This study emphasizes that Euler deconvolution applied to RTP-filtered data increases the interpretability of geological and structural contacts. The faulted zone (previously mapped by Texas A&M geology students) separating granite rocks from the Hickory sandstone has been mapped using the geophysical magnetic method. Results of the magnetic method have been compared and contrasted to results of GPR, EM and seismoelectric. The comparison shows that GPR and EM data acquired along the same profile as magnetic survey line 1 are in concordance as to fault location. Seismoelectric experiment at same targeted fault but different location indicates that the fault zone produces late arriving P-waves.

Gradient map (Figure 6.1 left) obtained from $B2-B1$ uses data from both sensors. The upward continuation was applied to remove some of the high frequency noise (see Figure 6.1 right). (Figure 6.2 left) shows the upward continued map and (Figure 6.2 right) shows the upward continued map with Euler deconvolution solution plotted. Also, the fault is interpreted based on the Euler deconvolution trend indicated by depth solutions greater than 3.5 m.

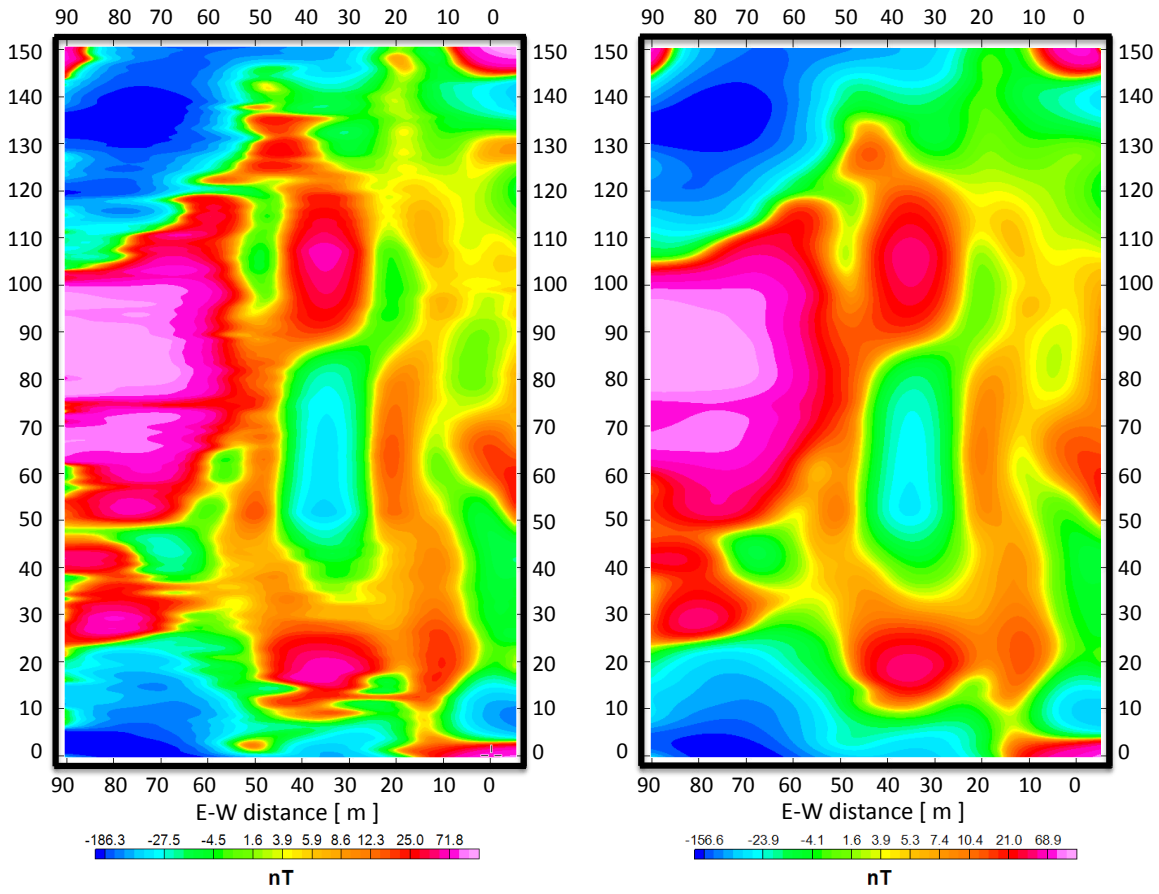

FIG. 6.1. (left) Gradient map of the study area. (right) Upward continued map at 2 m.

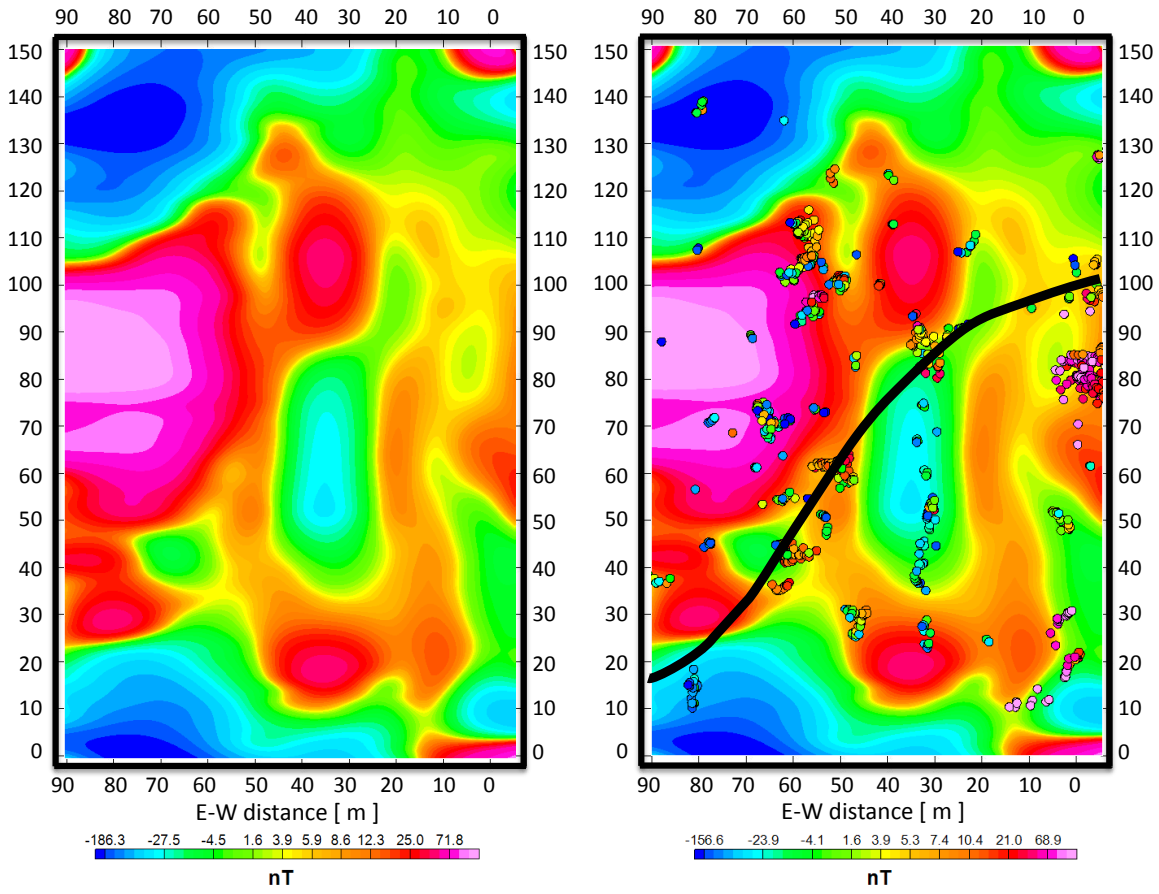

FIG. 6.2. Gradient map of the studay area. (left) Upward continued map at 2 m. (right) Euler deconvolution solutions overlain the gradient map and the fault interpreted.

REFERENCES

Barnes, V. E., and C. Bell, 1977, The moore hollow group of central Texas: Technical report, Texas Bureau of Economic Geology Report of Invesigation RI-88.

Blakely, R. J., 1995, Potential theory in gravity and magnetic applications: Cambridge University Press. Cambridge, UK.

Clark, D. A., 1997, Magnetic petrophysics and magnetic petrology: Aids to geological interpretation of magnetic surveys: Journal of Australian Geology & Geophysics Geophysics, **17**, 83–103.

Cohrs, F. F. R., 2012, Seismoelectric imaging of a shallow fault system employing fault guided waves: Ms thesis, Texas A&M University.

Cooper, G. R. J., 2004, [software] euler 1.15: University of Witwatersrand.

Dalziel, I. W. D., and S. Mosher, 2000, Laurentia-kalahari collision and the assembly of rodinia: Journal of Geology, **108**, 499–513.

Dormy, E., 2006, The origin of the Earth's magnetic field: Fundamental or environmental research?: Europhysics News, **37**, 22–25.

Durrheim, R. J., and G. R. J. Cooper, 1998, Euldep: A program for the euler deconvolution of magnetic and gravity data: Computers & Geosciences, **24**, 545–550.

Everett, M. E., 2013, Near surface applied geophysics: Cambridge University Press. (to appear). Cambridge, UK.

Finlay, C. C., S. Maus, C. Geggan, T. N. Bondar, and A. Chambodut, 2010, International geomagnetic reference field: The eleventh generation: Geophysical Journal International, **183**, 1216–1230.

Garland, G., 1979, The contributions of Carl Friedrich Gauss to geomagnetism: Historia Mathematica, **6**, 5 – 29.

Garland, G. D., 1971, Introduction to geophysics: Mantle, core, and crust: W. B. Saunders Company. Philadelphia, PA, USA.

Garrison, James, R., 1983, Geology of the Precambrian rocks of the Llano Uplift, central Texas : Field trip notes : Field trip notes for 1983 geological society of america south-central section field trip–central mineral region crystalline rocks,

Llano Uplift, central Texas, March 5-6, 1983: College of Geosciences, Texas A&M University.

Geosoft, 2012, [software] Oasis montaj 7.5 educational edition. Geosoft inc.

Grauch, V. J. S., M. R. Hudson, and S. A. Manor, 2000, Aeromagnetic signatures of intrabasinal faults, Albuquerque basin, New Mexico: Implications for layer thickness and magnetization: SEG Technical Program Expanded Abstracts, 363–366.

Harper, R., 2011, Geology of the Mcmillan ranch in Mason, Texas : An assessment of the nature of normal faults in the Mason area: Ms thesis, Texas A&M University.

Helper, M., 2006, Geologic map of the Mason mountain w.m.a, Mason co., Tx.

Hsu, S.-K., 2002, Imaging magnetic sources using Euler's equation: Geophysical Prospecting, **50**, 15–25.

Kearey, Philip. Brooks, M. H. I., 2002, An introduction to geophysical exploration, 3rd ed.: Blackwell Science. Oxford ;Malden, MA.

Lelievre, G. P., 2003, Forward modeling and inversion of geophysical magnetic data: Ms thesis, University of British Columbia.

Milligan, P., and P. Gunn, 1997, Enhancement and presentation of airborne geophysical data: Journal of Australian Geology & Geophysics, **17**, 63–75.

Murphy, B. C., 2014, Transient electromagnetic diffusion in a normal fault, Mason, Texas (to appear): Ms thesis, Texas A&M University.

Nasuti, A., C. Pascal, and J. Ebbing, 2012, Onshore–offshore potential field analysis of the Møre–Trøndelag fault complex and adjacent structures of mid Norway: Tectonophysics, **518–521**, 17–28.

Nelis, M. K., 1989, Grenville-age orogeny in the Llano Uplift of central Texas – deformation and metamorphsm of the Rough Ridge formation: Geological Society of America bulletin, **101**, 876–883.

Oruc, B., and H. H. Selim, 2011, Interpretation of magnetic data in the Sinop area of mid Black Sea, Turkey, using tilt derivative, Euler deconvolution, and discrete wavelet transform: Journal of Applied Geophysics, **74**, 194–204.

Reese, J. F., 2000, Mesoproterozoic chronostratigraphy of the southeastern Llano Uplift, central Texas: Geological Society of America bulletin, **112**, 278–291.

Reid, A. B., J. M. Allsop, H. Granser, A. J. Millett, and I. W. Somerton, 1990, Magnetic interpretation in three dimensions using Euler deconvolution: Geophysics, **55**, 80–91.

Saheel, A. S., A. R. Bin Samsudin, and U. Bin Hamzah, 2011, Mapping of faults in the Libyan Sirte basin by magnetic surveys: Sains Malaysiana, **40**, 853–864.

Sharma, P. V., 1997, Environmental and engineering geophysics: Cambridge University Press. Cambridge, UK.

Sheriff, R. E., 1989, Geophysical methods: Prince-Hall. New Jersey, USA.

Telford, W. M., L. P. Geldart, and R. E. Sheriff, 1990, Applied geophysics, 2nd ed.: Cambridge University Press. Cambridge, UK.

Teran, I. A. P., 2007, Stratal architecture and sedimentology of a portion of the upper Cambrian Hickory sandstone, central Texas, U.S.A: Ms thesis, Texas A&M University.

Thompson, D., 1982, Euldph: A new technique for making computer-assisted depth estimates from magnetic data: Geophysics, **47**, 31–37.

Tontini, F. C., L. Cocchi, and C. Carmisciano, 2006, Depth-to-the-bottom optimization for magnetic data inversion: Magnetic structure of the Latium volcanic region, Italy: Journal of Geophysical Research, **111**, B11104.

Whitehead, N., 2004, Geosoft technical note: Microlevelling using bi-directional gridding: Technical report, Geosoft inc.

Wilson, J. W., 2001, High-resolution stratigraphic and structural characterization of the fault-partitioned Hickory sandstone aquifer system, Mason county, central Texas: Ms thesis, Texas A&M University.

APPENDIX A

EULER DECONVOLUTION METHOD

A function f is considered homogeneous of degree n if it satisfies the Euler's equation [Thompson, 1982]:

$$(x - x_0)\frac{\partial f}{\partial x} + (y - x_0)\frac{\partial f}{\partial y} + (z - z_0)\frac{\partial f}{\partial z} = -N(B - f). \tag{A.1}$$

For magnetic field applications, the source of anomalous signal is centered at $P(x_0, y_0, z_0)$ in the form of $f(x_0, y_0, z_0) = G/r^n$ where $r = (x^2+y^2+z^2)^{1/2}$ and n is the degree of homogeneity. The structural index $n = N$ measures the rate of change with distance [Reid et al., 1990]. This parameter gives information about the geometry of the causative body (see Table 4.1). B is the base level background magnetic anomaly [Oruc and Selim, 2011]. The total magnetic field measurements $T(x_i, y_i, z_i)$ made at location $Q(x_i, y_i, z_i)$ with $i = 1, 2, 3...$to m measurements; therefore, T must satisfy the Euler's homogeneity equation of degree n. Taking the nth-order vertical derivative, according to Hsu [2002] it follows that:

$$(x_i - x_0)\frac{\partial}{\partial x}\left(\frac{\partial^n T}{\partial z^n}\right) + (y_i - y_0)\frac{\partial}{\partial y}\left(\frac{\partial^n T}{\partial z^n}\right) + (z_i - z_0)\frac{\partial}{\partial z}\left(\frac{\partial^n T}{\partial z^n}\right) = -N\left(\frac{\partial^n T}{\partial z^n}\right), \tag{A.2}$$

for all i, if $\mathbf{B}$ is a constant regional magnetic field, then $\Delta T_i = T(x_i, y_i, z_i) - \mathbf{B}$ also satisfies the Euler's equation of degree n; hence, in the case $n = 1$ the Euler solutions are:

$$(x_i - x_0)\frac{\partial^2 \Delta T_i}{\partial x \partial z} + (y_i - y_0)\frac{\partial^2 \Delta T_i}{\partial y \partial z} + (z_i - z_0)\frac{\partial^2 \Delta T_i}{\partial z^2} = -N\frac{\Delta T_i}{\partial z}. \tag{A.3}$$

For all i, the solutions to the equation A.3 are positioned at the calculated boarder of the susceptibility inhomogeneities [Hsu, 2002].

For all $i = 1, 2, 3...$ to m ΔT_i are measured and their derivatives with respect to (x, y, and, z) can be computed on the lefthand side of A.3. The location of of all measurements $Q(x_i, y_i, z_i)$ are known from the acquisition geometry. For any structural index N, the coordinates of the magnetic source $P(x_0, y_0, z_0)$ can be solved. The m measurements form the computational window (see Figure A.1).

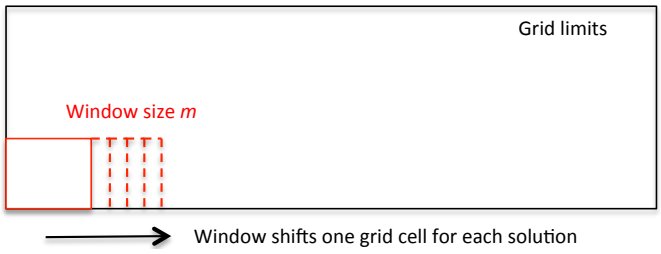

FIG. A.1. Illustration of the Euler deconvolution window size and movement direction.

The window size m should be: (a) large enough to include substantial variation of the field and field gradient, and (b) small enough not to include significant effects from multiple sources.

APPENDIX B

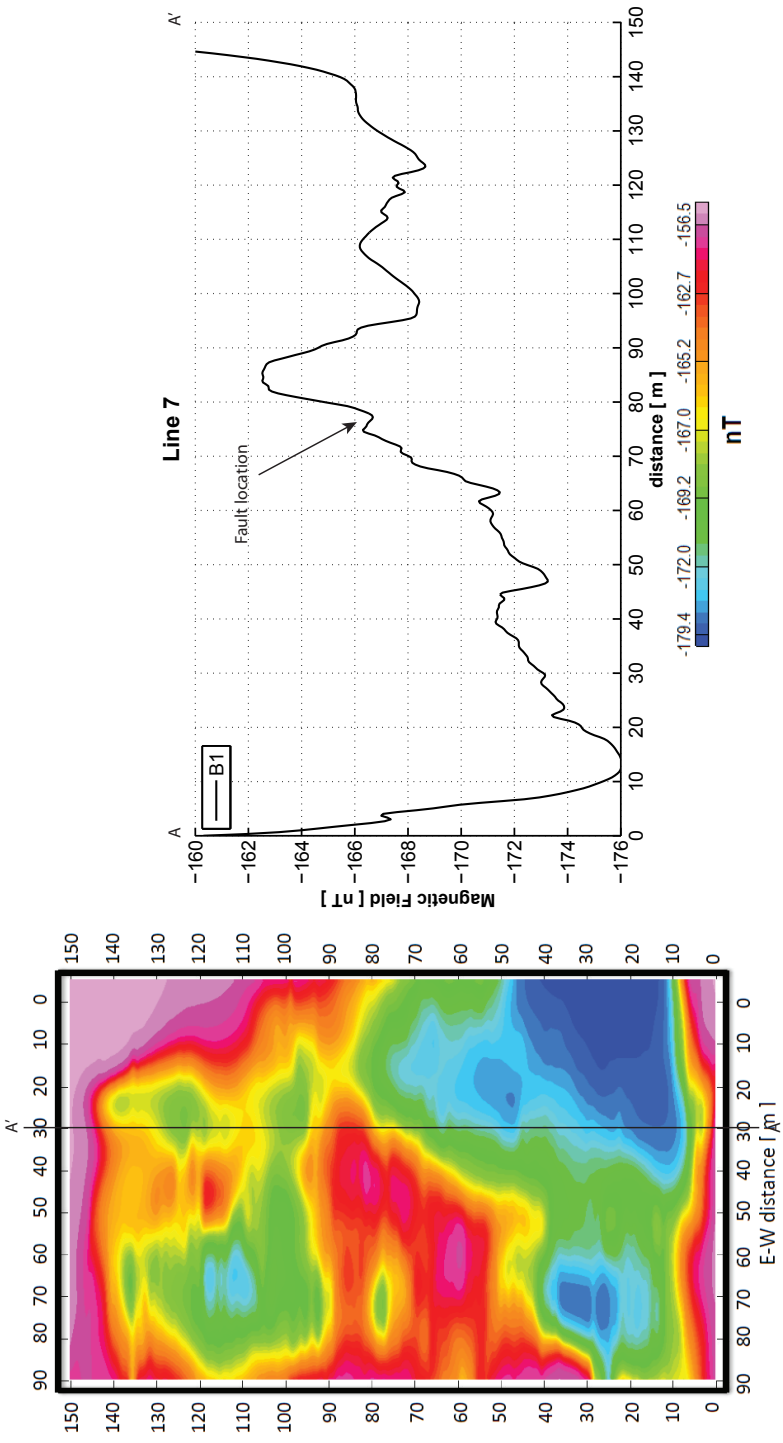

FIG. B.1. (left) Map of the total magnetic intensity B1. (right) Profile along line 7, from A to A' showing the fault location.

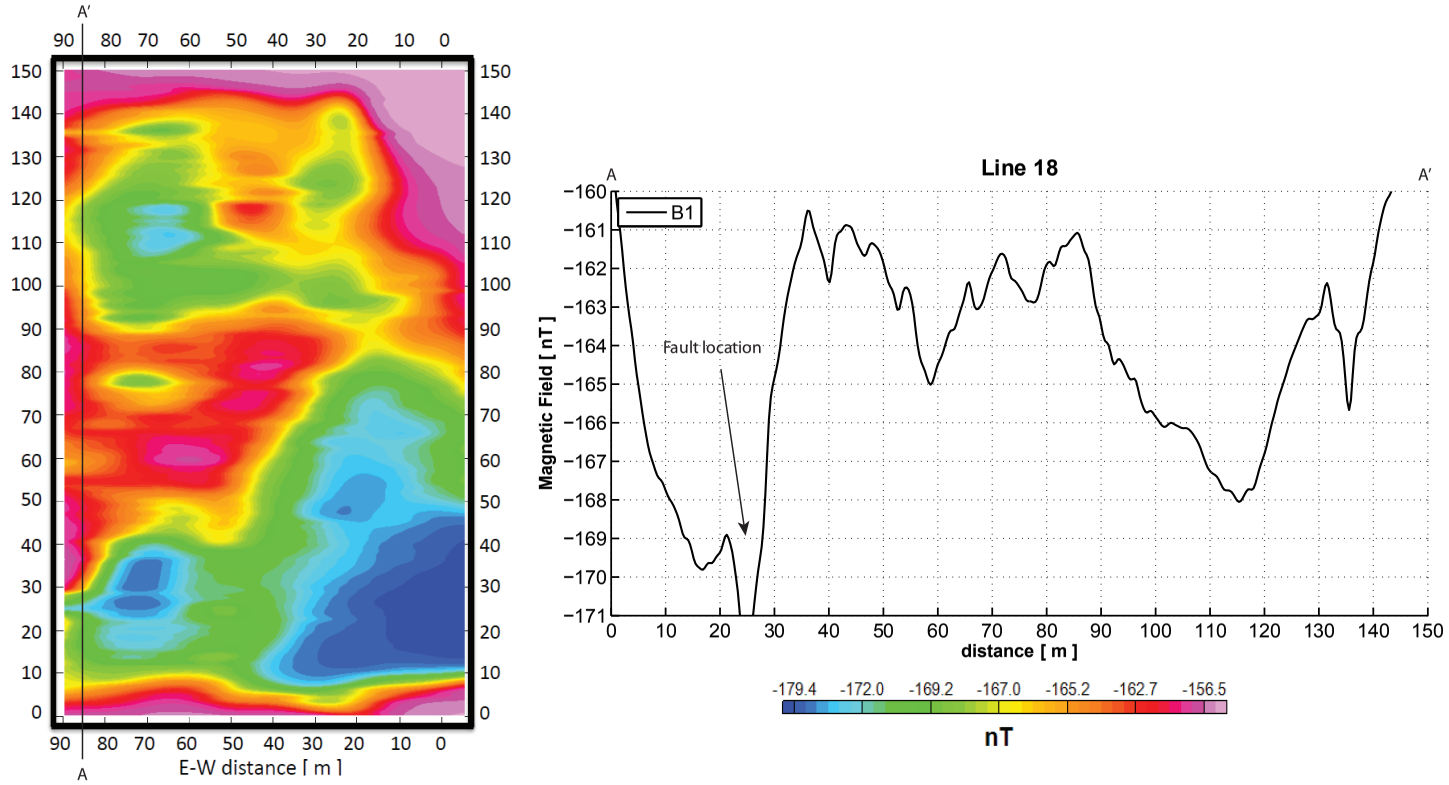

FIG. B.2. (left) Map of the total magnetic intensity B1. (right) Profile along line 18, from A to A' showing the fault location.